Journal of Luminescence 136 (2013) 221–239

Contents lists available at SciVerse ScienceDirect

Journal of Luminescence

journal homepage: www.elsevier.com/locate/jlumin

50th anniversary of the Judd–Ofelt theory: An experimentalist's view of the formalism and its application ☆

Markus P. Hehlen [a,*], Mikhail G. Brik [b], Karl W. Krämer [c]

[a] Materials Science & Technology Division (MST-7), Mailstop E549, Los Alamos National Laboratory, Los Alamos, NM 87545, USA
[b] Institute of Physics, University of Tartu, Riia 142, Tartu 51014, Estonia
[c] Department of Chemistry, University of Bern, Freiestrasse 3, CH-3012 Bern, Switzerland

ARTICLE INFO

Article history:
Received 30 July 2012
Received in revised form
15 October 2012
Accepted 19 October 2012
Available online 17 November 2012

Keywords:
Judd–Ofelt theory
4f transition intensities
Intermediate coupling wavefunctions
Lifetimes and branching ratios
Rare-earth spectroscopy

ABSTRACT

The theory on the intensities of 4f→4f transitions introduced by B.R. Judd and G.S. Ofelt in 1962 has become a centerpiece in rare-earth optical spectroscopy over the past five decades. Many fundamental studies have since explored the physical origins of the Judd–Ofelt theory and have proposed numerous extensions to the original model. A great number of studies have applied the Judd–Ofelt theory to a wide range of rare-earth-doped materials, many of them with important applications in solid-state lasers, optical amplifiers, phosphors for displays and solid-state lighting, upconversion and quantum-cutting materials, and fluorescent markers. This paper takes the view of the experimentalist who is interested in appreciating the basic concepts, implications, assumptions, and limitations of the Judd–Ofelt theory in order to properly apply it to practical problems. We first present the formalism for calculating the wavefunctions of 4f electronic states in a concise form and then show their application to the calculation and fitting of 4f→4f transition intensities. The potential, limitations and pitfalls of the theory are discussed, and a detailed case study of $LaCl_3:Er^{3+}$ is presented.

1. Introduction

It has been 50 years since the publication of the famous papers by Judd [1] and Ofelt [2] on the intensities of optical transitions in rare-earth ions. Their work, which we today refer to as the *Judd–Ofelt theory*, has become a centerpiece of rare-earth spectroscopy as evidenced by the more than 3500 citations each of Judd's and Ofelt's papers. The great appeal of the Judd–Ofelt theory is in its ability to predict oscillator strengths in absorption and luminescence, luminescence branching ratios, excited-state radiative lifetimes, energy-transfer probabilities, and estimates of quantum efficiencies by using only three parameters, $\Omega_{(\lambda)}$ ($\lambda=2,4,6$). Computational power is cheap today, and this easily masks the complex and diverse mathematical concepts as well as the highly laborious calculations underlying the Judd–Ofelt theory. Its development in the absence of computers in the late 1950s and early 1960s was an exquisite feat not only by Judd and Ofelt but also by the many that laid the foundation for their work. The introduction of the Judd–Ofelt theory 50 years ago has been a true and lasting breakthrough for the field of rare-earth spectroscopy.

Brian Judd's interest in the topic was first sparked while he was a graduate student at Oxford University in the early 1950s [3,4]. There, his roommate D. Bijl gave him a copy of the 1947 thesis of Hoogschagen from the University of Leiden on the absorption spectra of the rare earths in aqueous solution [5,6], and he also immersed himself in the earlier work by van Vleck on the origin of optical transitions in rare-earths [7,8]. In Judd's 1955 thesis on rare-earth double-nitrates, however, he omitted his work on the transition intensities because it seemed too speculative to him at the time [3]. In subsequent years, Judd learned about the tensorial techniques and the theory of Lie groups that Racah had developed in the late 1940s. He started applying Racah's mathematical and group theoretical principles to the rare earths. During a yearlong stay with Eugene Wigner at the University of Chicago, he succeeded in calculating the reduced matrix elements of the $U^{(k)}$ ($k=2,4,6$) single-electron tensor (see Section 2.2), which characterizes electric-dipole induced 4f↔4f transition intensities. Meanwhile, Brian Wybourne at Johns Hopkins University published the diagonalization of the spin–orbit matrices of Nd^{3+} and Er^{3+} in the early 1960s [9,10]. This allowed Judd to use the respective wavefunctions for a more accurate calculation of transition intensities in terms of three intensity parameters, which Axe later denoted as $\Omega_{(\lambda)}$ [11] and we today refer to as the *Judd–Ofelt intensity parameters*. Judd's work during this decade led to his seminal 1962 paper on the optical absorption intensities of rare-earth ions [1] and his 1963 book on operator techniques in atomic spectroscopy [12]. Independently and in parallel, Wybourne's student George Ofelt had developed

* Corresponding author. Tel.: +1 505 665 1737.
E-mail address: hehlen@lanl.gov (M.P. Hehlen).
☆ Los Alamos National Laboratory Unclassified Release LA-UR-12-23438.

0022-2313/$ - see front matter © 2012 Elsevier B.V. All rights reserved.
http://dx.doi.org/10.1016/j.jlumin.2012.10.035

a model of the intensities of crystal spectra of rare-earth ions [2] that was structurally similar to that of Judd. Together, Judd's and Ofelt's 1962 papers became known as the *Judd–Ofelt theory*, a term that was first coined by Weber in 1967 [13]. The theory however was already being applied in the mid-1960s by Axe [11] and Krupke et al. [14,15] to analyze the optical spectra of rare-earth-doped ethylsulfates, yttria, and LaF_3.

In the five decades since, there have been hundreds of studies using the Judd–Ofelt theory to analyze optical spectra of all the rare earths in a plethora of compounds. There have also been various important advances on the theoretical side that have led to several modified Judd–Ofelt theories over the years. A rigorous derivation of the mathematical foundations of the Judd–Ofelt theory and a comprehensive survey of its practical applications to rare-earth-doped materials is clearly beyond the scope of a review article. Such extensive reviews have been given in the past [16,17], and they serve as a valuable resource for more detailed studies of the topic. Instead, this paper takes the view of the experimentalist who is interested in appreciating the basic concepts, implications, assumptions, and limitations of the theory in order to properly apply it to practical problems. The simplicity and great predictive capability of the Judd–Ofelt theory has spurred its widespread use; this simplicity however is quite deceptive. One often overlooked fact is that the theory builds on reduced matrix elements of the $U^{(k)}$ and $L+gS$ tensor operators (see Section 2.2), which in turn directly depend on the wavefunctions of the involved electronic states. Therefore, the proper application of the Judd–Ofelt theory first requires the calculation of high-quality wavefunctions for the material system at hand which then serve as the basis for the Judd–Ofelt intensity calculation. In fact, the calculation of wavefunctions and corresponding reduced matrix elements is usually the most challenging and laborious aspect of using the Judd–Ofelt theory. Many studies however have glanced over this fact and have used tabulated reduced matrix elements that were derived for other material systems. While this zero-order approach often yields results of the correct order of

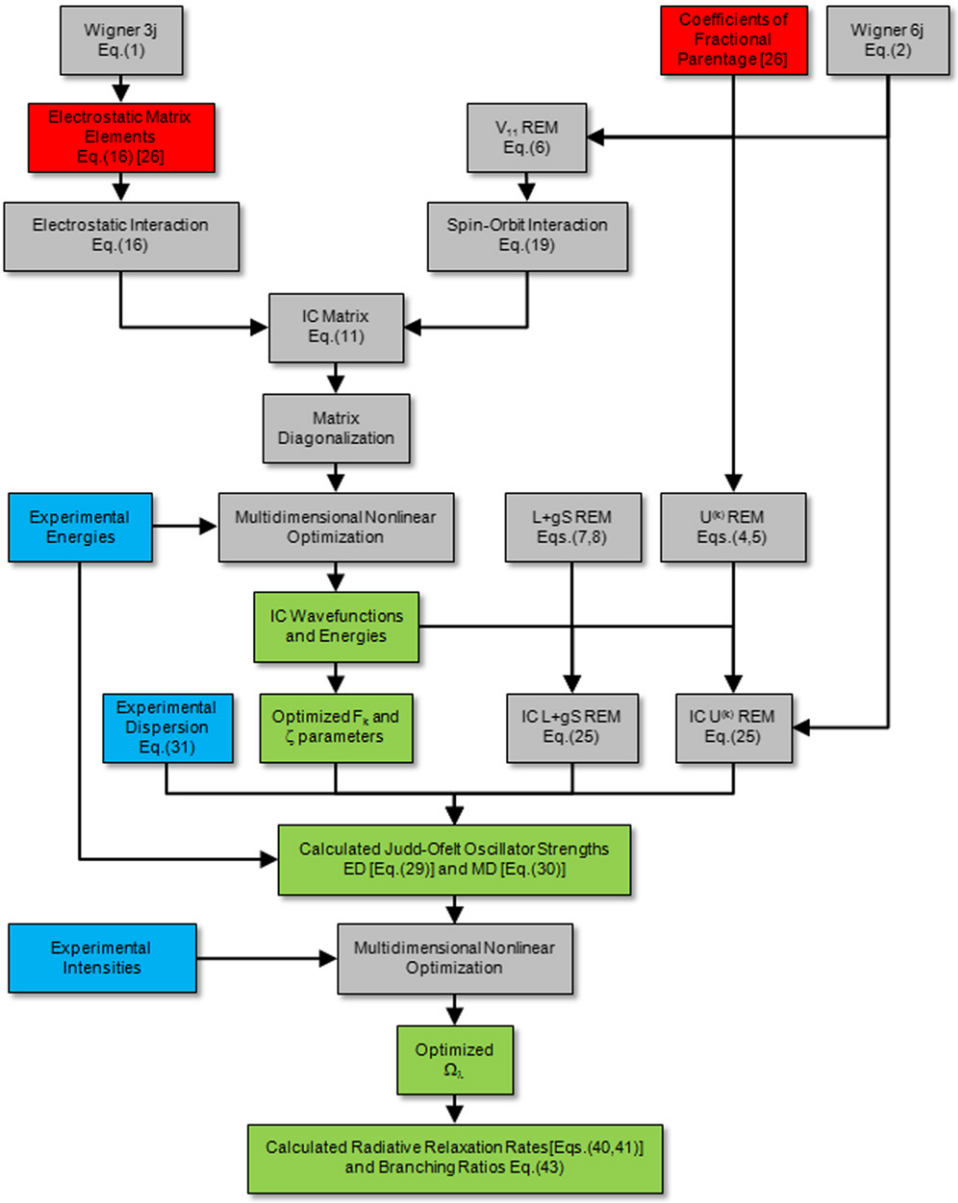

Fig. 1. Flowchart for the calculation of 4f intermediate coupling (IC) wavefunctions, Judd–Ofelt intensity parameters, and derived quantities. The colors denote tabular inputs (red), experimental inputs (blue), numerical procedures (grey), and outputs (green). References to equations and tabular works are indicated. REM denotes reduced matrix element.

magnitude, it generally fails to produce results that allow for quantitative comparison with and physically correct interpretation of the experiment. Other aspects that warrant closer examination are the labeling conventions for and assignments of 4f excited states, the effect of refractive index dispersion, and the type of least-squares fitting used in the calculations.

In this paper we present a concise collection of all equations needed for calculating 4f wavefunctions in the intermediate coupling approximation (Section 2), describe the essence of the basic Judd–Ofelt theory and its application to experimental data (Section 3), and illustrate the approach with the exemplary case of $LaCl_3$:Er^{3+} (Section 4). Our goal is to provide the reader with a useful tool set for practical work and, together with an extensive bibliography, offer a gateway into the more comprehensive original literature.

2. Theoretical background

To fully appreciate the potential and limitations of the Judd–Ofelt theory as well as to properly apply the theory to practical problems, it is important to gain a basic understanding of the larger context of the Judd–Ofelt theory, the nature of 4f electronic wavefunctions, and the associated calculus. While the underlying quantum mechanics of atomic spectra in general and of rare earths in particular had been solved by the 1960s [12,18–25], the respective original mathematical texts are often difficult to grasp for the experimentalist. As a result, many applied rare-earth spectroscopy studies resorted to applying existing computer codes, sometimes with insufficient appreciation for the limitations of the theory and the physical meaning of characteristic parameters. The purpose of this section, therefore, is to present the essence of the formalism in a concise format suited for the practical application of the theory. It is beyond the scope of this review to cover many of the more fundamental quantum-mechanical and group-theoretical aspects or to even attempt to provide rigorous mathematical proofs of the formulae. We provide here, however, a self-consistent set of all the equations necessary for the calculation of 4f wavefunctions and oscillator strengths of 4f↔4f transitions in the context of the Judd–Ofelt theory. The interested reader may find this section a useful starting point for the study of the original literature. The flowchart shown in Fig. 1 captures the structure of the calculations and will serve as a guide throughout the following sections.

2.1. Electronic states of the $[Xe]4f^N$ electron configurations

The 3+ oxidation state is by far the most common for rare-earth (RE) ions in condensed matter. Some of the rare earths also form stable compounds in the 2+ (*e.g.* Nd, Sm, Eu, Dy, Tm and Yb) and 4+ (*e.g.* Ce, Pr, Nd, Tb and Dy) oxidation states. Here we shall only focus on RE^{3+} ions. Their electron configuration is $[Xe]4f^N$, where N runs from 1 (Ce^{3+}) to 13 (Yb^{3+}) along the series of RE ions. The 4f-orbitals are empty for La^{3+} ($N=0$) and filled for Lu^{3+}

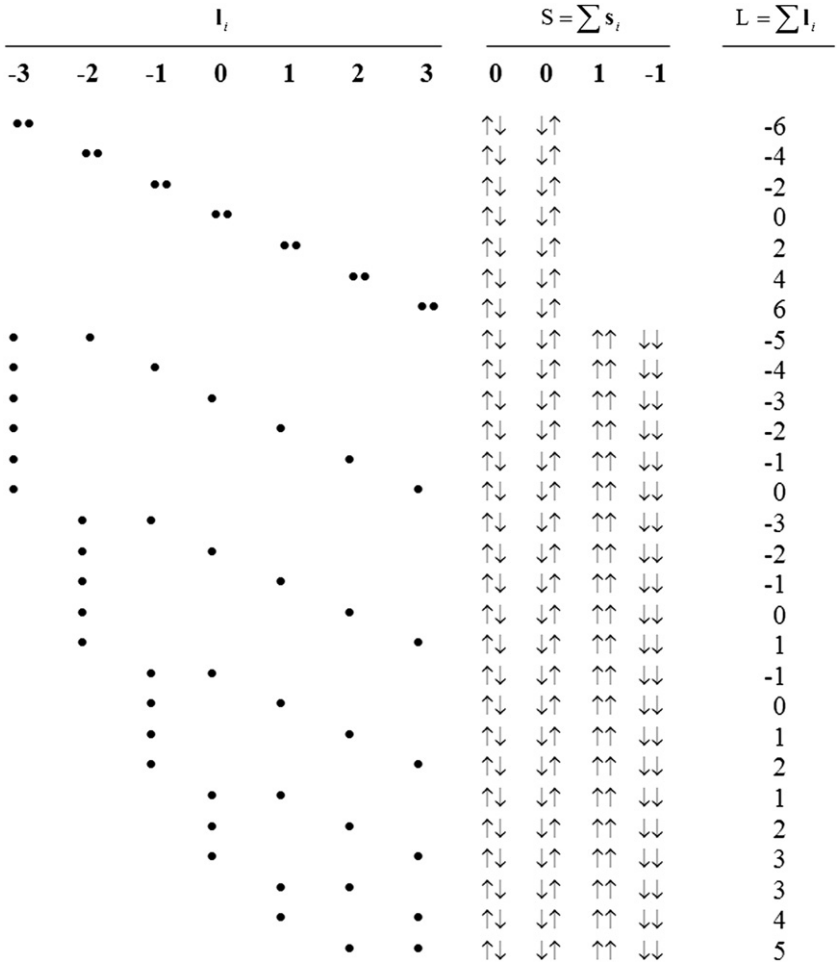

Fig. 2. *L–S* coupling for the $[Xe]4f^2$ electron configuration. There are 28 ways of arranging the two electrons (black dots) among the 7 possible l_i values, and for each of those l_i arrangements there are two or four possible ways of arranging the spins s_i. This results in a total of 98 (s_i, l_i) microstates with total spin $S=\sum s_i=-1,\ldots,1$ and orbital angular momentum $L=\sum l_i=-6,\ \ldots,\ 6$.

($N=14$), and these ions therefore do not have any 4f↔4f transitions. For a given [Xe]4f^N electron configuration, one can consider the N 4f electron spins s_i and the N 4f electron orbital angular momenta l_i to combine *separately* to form a total spin angular momentum $S=\sum s_i$ with a quantum number $M_S=-S, \ldots, S$ and total orbital angular momentum $L=\sum l_i$ with a quantum number $M_L=-L, \ldots, L$, respectively, as a result of the electrostatic (Coulomb) interaction between the 4f electrons. The fact that electrons are fermions (particles having half-integer spin) restricts the possible (s_i, l_i, m_{s_i} and m_{l_i}) combinations according to Pauli's exclusion principle. For a single 4f electron, one has $m_{s_i}=\pm 1/2$ and $m_{l_i}=-3,\ldots,3$ and, thus, for a 4f^N electron system the maximum values $M_S=-N/2,\ldots,N/2$ and $M_L=-3N, \ldots, 3N$. One can construct an L–S matrix by finding all possible combinations of m_{s_i} and m_{l_i} and tallying up the respective M_S and M_L. This is shown in its entirety in Fig. 2 for the example of the [Xe]4f^2 electron configuration, which consists of a total of 98 possible arrangements (microstates) of the spin and orbital angular momenta. The number N_{states} of possible microstates for a [Xe]4f^N electron configuration is given by $N_{\text{states}}=14!/N!(14-N)!$. All combinations that give rise to the same angular momentum quantum numbers are denoted by the term symbol ^{2S+1}L. Here the letter symbol L=S, P, D, F, G, H, I, K, L, M, N, O and Q, stands for L=0, 1, 2, 3, 4, 5, 6, 7, 8, 9, 10, 11 and 12, respectively, and $(2S+1)$ is the *spin multiplicity* which is referred to as a singlet, doublet, triplet, quartet, quintet, for $(2S+1)$=1, 2, 3, 4, 5, …. The ^{2S+1}L terms are then found by successively subtracting the corresponding microstates from the L–S matrix (see Fig. 3). This procedure can be used to find the ^{2S+1}L terms of any electron configuration, however it quickly becomes very laborious as the number of f-electrons increases. Hund's rule determines the ground term of any electron configuration as having both the greatest spin multiplicity and the greatest value of L (of the terms with the greatest spin). Note that a [Xe]4f^N ($N>7$) electron configuration produces the same ^{2S+1}L terms as the respective conjugate [Xe]4f^{14-N} electron configuration because it can simply be viewed as consisting of $(14-N)$ 4f holes. That is, the types of ^{2S+1}L terms are mirrored about the 4f^7 electron configuration, however not their energy sequence, and only the ground terms are the same for the conjugate configurations. For $3\le N\le 11$ there are some ^{2S+1}L terms having the same L and S and, therefore, a sequential index τ, often called *seniority quantum number*, is added to distinguish these terms, *i.e.* $^{2S+1}L(\tau)$. It is conventional to follow the respective group-theoretical definitions introduced by Racah [21] and tabulated by Nielsen and Koster [26]. For example, the [Xe]4f^3 electron configuration of Nd^{3+} produces two terms with $S=1/2$ and $L=5$, and the respective terms are labeled ^{2}H(1) and ^{2}H(2). These terms differ in the so-called *parent* terms of the preceding [Xe]4f^2 electron configuration (see Section 2.2), which give rise to these ^{2}H(1) and ^{2}H(2) terms after the third electron is added.

The next contribution to consider is the spin–orbit interaction, which results from the interaction of the intrinsic magnetic moment of the electron with the magnetic field created by its motion around the nucleus [22]. The magnitude of the spin–orbit interaction increases with the nuclear charge as Z^4 [22]. While spin–orbit coupling (H_{so}) is small compared to the electrostatic interaction between the 4f electrons (H_{e}) for the light transition metals, it becomes comparable to H_{e} for the rare earths. As the relative magnitude of the spin–orbit coupling increases, both S and L cease to be good quantum numbers, and the total angular momentum J must be introduced. There are two extreme approaches to accomplish this coupling of L and S to form the resultant J. For $H_{\text{so}} << H_{\text{e}}$, the L–S (or Russel–Saunders) coupling scheme is appropriate where the spin and orbital angular momenta couple *separately*, *i.e.* $S=\sum s_i$ and $L=\sum l_i$ (as shown in Figs. 2 and 3), and the total angular momentum is obtained as

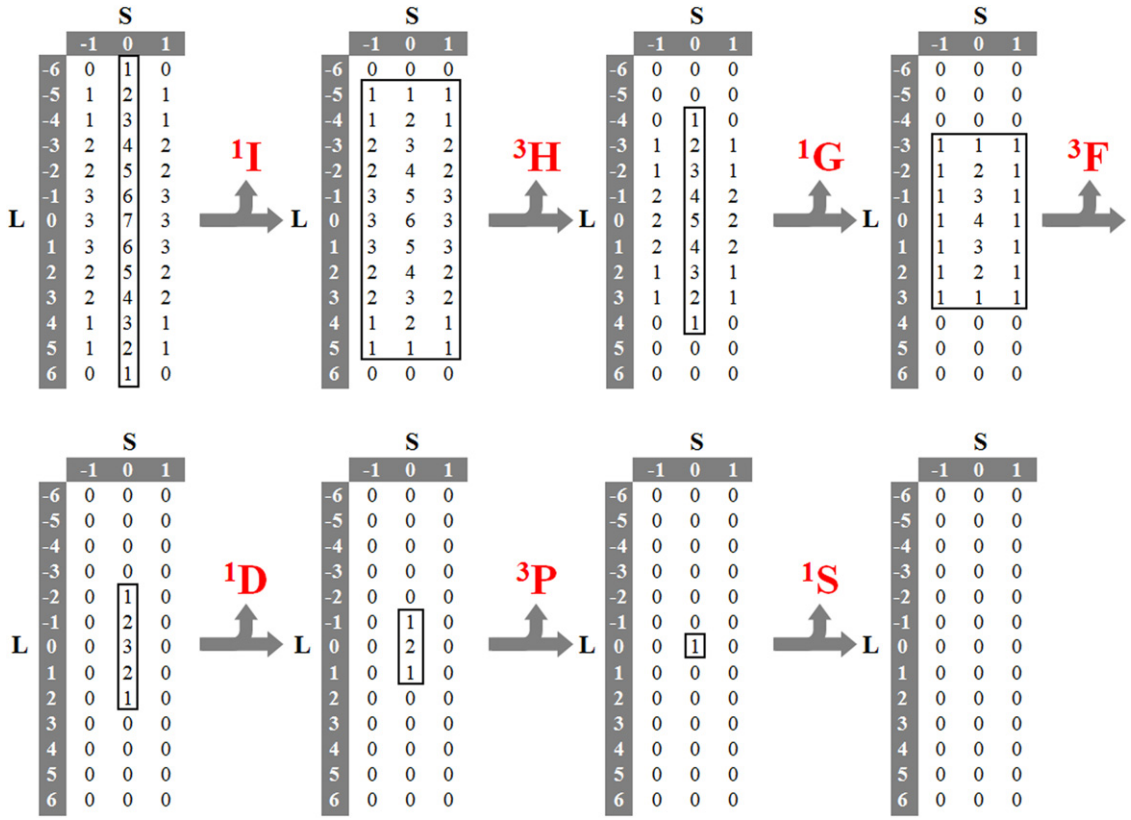

Fig. 3. Derivation of all L–S terms of the [Xe]4f^2 electron configuration. The first L–S matrix summarizes all 98 (s_i, l_i) microstates found in Fig. 2. The individual ^{2S+1}L terms are then obtained by successively subtracting the corresponding microstates (denoted by black frames).

Table 1
Number of ^{2S+1}L terms, $^{2S+1}L_J$ multiplets, and $^{2S+1}L_J(M_J)$ crystal-field levels in trivalent rare-earth ions (RE^{3+}) with [Xe]$4f^N$ electron configuration. The electrostatic interaction between the 4f electrons gives rise to SL terms which further split into SLJ multiplets under the influence of the spin-orbit interaction. They split even further into SLJM crystal-field levels under the influence of a static crystal field and/or magnetic field [41].

	$Ce^{3+}(Yb^{3+})$	$Pr^{3+}(Tm^{3+})$	$Nd^{3+}(Er^{3+})$	$Pm^{3+}(Ho^{3+})$	$Sm^{3+}(Dy^{3+})$	$Eu^{3+}(Tb^{3+})$	Gd^{3+}
4f electrons (4f holes)	1	2	3	4	5	6	7
SL	1	7	17	47	73	119	119
SLJ	2	13	41	107	198	295	327
SLJM	14	91	364	1001	2002	3003	3432

$J=L+S$. For $H_{so} >> H_e$, the *jj* coupling scheme applies where the individual spins and orbital angular momentum are coupled first, *i.e.* $j_i=s_i+l_i$, and the total angular momentum is then obtained as $J=\sum j_i$. The rare earths represent an "intermediate coupling" case where $H_{so} \approx H_e$. The *L–S* coupling scheme is commonly used for RE^{3+}. The spin–orbit interaction causes the ^{2S+1}L terms of a [Xe]$4f^N$ configuration to split into several $^{2S+1}L_J$ multiplets with different energies, where $J=|L-S|,|L-S+1|,\ldots,|L+S|$. The terminology used here is that of Judd [12]. It is worthwhile noting that for the less-than-half filled 4f electron configurations, the energies of the J states within the same $^{2S+1}L_J$ manifold increase with increasing J, whereas the trend is inverted for the more-than-half filled configurations. For example, for the Pr^{3+} ion ($4f^2$) the ^3H_J ($J=4,5,6$) levels in order of increasing energy are $^3H_4$, $^3H_5$, $^3H_6$. For the conjugate $4f^{12}$ configuration (Tm^{3+}), the same levels are ordered as $^3H_6$, $^3H_5$, $^3H_4$. Table 1 summarizes the electron configurations, number of ^{2S+1}L terms, and the number of $^{2S+1}L_J$ multiplets for all RE^{3+} ions. The treatment so far only yields the type of $^{2S+1}L_J$ multiplets for a given [Xe]$4f^N$ electron configuration but not their energy sequence, which requires a quantitative evaluation of the electrostatic and spin–orbit interactions. This will be the task in Section 2.3.

The $^{2S+1}L_J$ multiplets derived above represent the energy levels of the RE^{3+} ion in the spherical symmetry of free space, the so-called "free ions". A further and much smaller energy splitting occurs when the RE^{3+} ion is placed into the lower-symmetry electrostatic field that is produced by the charges of the neighboring ions in a solid. Depending on the exact point symmetry of the electrostatic field at the RE^{3+} site, a crystal-field splitting occurs which lifts some or all of the $(2J+1)$ degeneracy in each of the $^{2S+1}L_J$ multiplets. Note that independent of the point symmetry of the electric field, odd-electron systems will retain a minimum of two-fold degeneracy in each crystal-field level due to Kramer's degeneracy [27] which can only be lifted by a magnetic field. In contrast, the $(2J+1)$ degeneracy can be completely lifted in even-electron systems by a crystal-field of sufficiently low symmetry. The Judd–Ofelt theory was originally formulated within the context of $^{2S+1}L_J$ multiplets. We shall therefore neglect crystal-field interactions in the following and restrict the discussion to $^{2S+1}L_J$ multiplets and transitions between them. We will see in Section 3, however, that crystal-field interactions are the essential ingredient that gives intensity to the otherwise parity-forbidden $4f \rightarrow 4f$ transitions.

2.2. Wigner symbols and reduced matrix elements of tensor operators

The previous section has illustrated that the systems of interest comprise multiple 4f electrons. At the heart of the formalism therefore lies the coupling of angular momenta of single electrons in order to construct eigenstates of the multi-electron system. For example, two 4f electrons, each with a well-defined angular momentum of $l=3$, interact by Coulomb forces to form a total angular momentum of the two-electron system. Likewise, the spin and orbital angular momentum of a 4f electron can couple by spin–orbit interaction. The mathematical treatment of coupling two angular momenta gives rise to the so-called Wigner 3-j symbol, which is related to the Clebsch–Gordan coefficient [25] and which is given by [19,28]

$$\begin{pmatrix} a & b & c \\ \alpha & \beta & \gamma \end{pmatrix} = (-1)^{a-b-\gamma}\sqrt{\Delta(a,b,c)}\sqrt{(a+\alpha)!(a-\alpha)!(b+\beta)!(b-\beta)!(c+\gamma)!(c-\gamma)!} \times \sum_t \frac{(-1)^t}{x(t)} \quad (1)$$

where $x(t)=t!(c-b+t+\alpha)!(c-a+t-\beta)!(a+b-c-t)!(a-t-\alpha)!(b-t+\beta)!$, the sum is taken over all t for which all factorials in $x(t)$ are ≥ 0, and the triangle coefficient is given by $\Delta(a,b,c)=(a+b-c)!(a-b+c)!(-a+b+c)!/(a+b+c+1)!$ [29]. Coupling three angular momenta gives rise to the so-called Wigner 6-j symbol [24], which is a sum of products of 3-j symbols and evaluates to [12,30]

$$\begin{Bmatrix} j_1 & j_2 & j_3 \\ J_1 & J_2 & J_3 \end{Bmatrix} = \sqrt{\Delta(j_1,j_2,j_3)\Delta(j_1,J_2,J_3)\Delta(J_1,j_2,J_3)\Delta(J_1,J_2,j_3)} \times \sum_t \frac{(-1)^t(t+1)!}{f(t)} \quad (2)$$

where $\Delta(a,b,c)$ is the aforementioned triangle coefficient, the sum is taken over all t for which all factorials in $f(t)$are ≥ 0, and

$$f(t)=(t-j_1-j_2-j_3)!(t-j_1-J_2-J_3)!(t-J_1-j_2-J_3)!(t-J_1-J_2-j_3)! \times (j_1+j_2+J_1+J_2-t)!(j_2+j_3+J_2+J_3-t)!(j_3+j_1+J_3+J_1-t)!$$

The various interactions in the multi-electron system are described by tensor operators $T_q^{(k)}$, which transform like the spherical harmonics $Y_{k,q}(\theta,\phi)$ (see Section 2.3) [12]. The associated theory of tensor operators has been pioneered by Racah [19,21]. Throughout the calculation of RE^{3+} energy levels and transition intensities, the need arises to evaluate matrix elements of various tensor operators that act on only one part of the system, such as only the orbital angular momentum or only on the spin. Application of the Wigner–Eckart theorem [24,31] facilitates the calculation of those matrix elements enormously by making use of so-called *reduced matrix elements* (RME). The mathematical formulation of this theorem is:

$$\langle j'm'\alpha'|T_q^{(k)}|jm\alpha\rangle = (-1)^{j'-m'}\begin{pmatrix} j' & k & j \\ -m' & q & m \end{pmatrix}\langle j'\alpha'||T^{(k)}||j\alpha\rangle \quad (3)$$

where $T_q^{(k)}$ is a tensor operator of rank k whose matrix element is calculated between two states $\langle j'm'\alpha'|$ and $|jm\alpha\rangle$, with the j', j and m', m being the quantum numbers of the total momenta and their z-components, respectively. All other (if needed) quantum numbers are denoted by α and α'. The double bar entry on the right-hand side is the RME, which depends neither on the magnetic quantum numbers m', m nor on the q-component of the tensor operator $T_q^{(k)}$. The main advantage of the Wigner–Eckart theorem is that any matrix element of a given tensor operator can be

calculated in a simple way by multiplying the Wigner 3j-symbol in Eq. (3) with the corresponding RME, which has to be calculated only once for a particular combination of $T_q^{(k)}$, j', and j.

Three tensor operators $U^{(k)}$, $V^{(1x)}$, and $L+gS$ and their respective reduced matrix elements are of particular importance for spectroscopic calculations. $U^{(k)}$ arises in the calculation of electric-dipole transition intensities. Its reduced matrix element is given by [25]

$$\langle l^N SL||U^{(k)}||l^N SL'\rangle = N\sqrt{(2L+1)(2L'+1)} \times \sum_{\psi(l^{N-1})} \left(l^{N-1}\overline{SL}\middle|l^N SL\right) \begin{Bmatrix} L & l & \overline{L} \\ l & L' & k \end{Bmatrix} (-1)^{\overline{L}+L+l+k} \tag{4}$$

Here one makes use of the concept of fractional parentage, which was introduced by Racah in 1943 [20]. This elegant approach expresses the states of a $4f^N$ electron configuration as linear combinations of the states of the preceding $4f^{N-1}$ electron configuration angular-momentum-coupled to one additional 4f electron. The coefficients of these linear combinations are the coefficients of fractional parentage, $\left(l^{N-1}\overline{SL}|l^N SL\right)$, and they have been explicitly calculated by Nielsen and Koster [26] within the definitions of Racah [20]. In Eq. (4), the sum extends over all parent states of $\langle l^N SL|$, which are denoted by $\psi(l^{N-1})$ and the respective quantum numbers $\overline{S}$ and $\overline{L}$. Note that for the conjugate $4f^{14-N}$ electron configuration one has $\langle l^{14-N}SL||U^{(k)}||l^{14-N}S'L'\rangle = -(-1)^k\langle l^N SL||U^{(k)}||l^N S'L'\rangle$ [26]. Coupling S and L to J then yields [32]:

$$\langle l^N SLJ||U^{(k)}||l^N SL'J'\rangle = (-1)^{S+L'+J+k}\sqrt{(2J+1)(2J'+1)} \times \begin{Bmatrix} J & J' & k \\ L' & L & S \end{Bmatrix} \langle l^N SL||U^{(k)}||l^N SL'\rangle \tag{5}$$

The $V^{(1x)}$ tensor operator arises in the calculation of matrix elements of the spin–orbit interaction operator, and its reduced matrix element is given by [25]:

$$\langle l^N SL||V^{(1x)}||l^N S'L'\rangle = N\sqrt{s(s+1)(2s+1)(2S+1)(2L+1)(2S'+1)(2L'+1)} \times \sum_{\psi(l^{N-1})} \left(l^{N-1}\overline{SL}\middle|l^N SL\right) \begin{Bmatrix} S & S' & 1 \\ s & s & \overline{S} \end{Bmatrix} \begin{Bmatrix} L & L' & x \\ l & l & \overline{L} \end{Bmatrix} (-1)^{\overline{S}+\overline{L}+S+L+s+l+x+1} \tag{6}$$

where $s=1/2$ and $l=3$ (for f-electrons). Note that for the conjugate $4f^{14-N}$ electron configuration one has $\langle l^{14-N}SL||V^{(1x)}||l^{14-N}S'L'\rangle = (-1)^x\langle l^N SL||V^{(1x)}||l^N S'L'\rangle$ [26].

Finally, reduced matrix elements of $L+gS$ arise in the calculation of magnetic-dipole transition intensities, and they are given by [25]

$$\langle l^N SLJ||L+gS||l^N SLJ'\rangle = g\sqrt{J(J+1)(2J+1)} \tag{7}$$

for $J'=J$ and

$$\langle l^N SLJ||L+gS||l^N SL(J-1)\rangle = (g-1)\sqrt{\frac{(S+L+J+1)(J+L-S)(J+S-L)(S+L-J+1)}{4J}} \tag{8}$$

for $J'=J-1$, where $g=2.002319304362$ which is the g-factor of the electron.

2.3. The intermediate coupling approximation

The electrostatic ($\hat{H}_e$) and spin–orbit ($\hat{H}_{so}$) interactions are dominant in RE^{3+} ions. Detailed studies of atomic and crystal-field interactions in RE^{3+}-doped solids have shown that the combined magnitude of $\hat{H}_e$ and $\hat{H}_{so}$ amounts to 80–90% of all interactions [33–39]. The other 10–20% are due to higher-order atomic (*e.g.* inter-configurational and two-body spin–orbit interactions) and crystal-field interactions. These higher-order contributions are important if a quantitative description of crystal-field energy levels and transitions between them is sought. In the context of the Judd–Ofelt theory however, considering only $\hat{H}_e$ and $\hat{H}_{so}$ offers a useful first-order description known as the intermediate coupling approximation [40].

The Hamilton operator corresponds to the total energy of the system and in the intermediate coupling approximation can be written as

$$\hat{H} = \hat{H}_e + \hat{H}_{so} \tag{9}$$

The energies, E, of the respective $^{2S+1}L_J$ multiplets are then found by solving the time-independent Schrödinger equation:

$$\hat{H}\Psi = E\Psi \tag{10}$$

where $\Psi=(\Psi_1, \ldots, \Psi_z)$ represents the wavefunctions of all z $^{2S+1}L_J$ multiplets of the 4f electron configuration at hand (see Table 1). This multi-electron Schrödinger equation has no exact solution. The common approach for solving Eq. (10) is to use the central-field approximation [12,25] in which each electron is assumed to move independently in the field of the nucleus and an averaged spherical central field produced by the other electrons, $-U(r_i)/e$. This allows expression of the wavefunctions Ψ in terms of the spherical harmonics $Y_{l,m_l}(\theta,\phi)$, *i.e.* $\Psi = R_{nl}(r)Y_{l,m_l}(\theta,\phi)$, where $R_{nl}(r)$ is a radial function that depends on $U(r)$ [12]. It is illustrative to write the intermediate coupling eigenvalue equation [Eq. (10)] in explicit matrix form:

$$\begin{bmatrix} \hat{H}_{11} & \hat{H}_{12} & \cdots & \hat{H}_{1z} \\ \hat{H}_{21} & \hat{H}_{22} & \cdots & \hat{H}_{2z} \\ \vdots & \vdots & \ddots & \vdots \\ \hat{H}_{z1} & \hat{H}_{z2} & \ldots & \hat{H}_{zz} \end{bmatrix} \begin{bmatrix} \Psi_1 \\ \Psi_2 \\ \vdots \\ \Psi_z \end{bmatrix} = \begin{bmatrix} E_1 & & & \\ & E_2 & & \\ & & \vdots & \\ & & & E_z \end{bmatrix} \begin{bmatrix} \Psi_1 \\ \Psi_2 \\ \vdots \\ \Psi_z \end{bmatrix} \tag{11}$$

where each matrix element is given by $\hat{H}_{ij} = \hat{H}_e^{(ij)} + \hat{H}_{so}^{(ij)}$ and the matrix is square ($z \times z$) and symmetrical, *i.e.* $\hat{H}_{ij} = \hat{H}_{ji}$. Recall that this general type of eigenvalue equation is solved by calculating each matrix element $\hat{H}_{ij}$ of the Hamiltonian matrix $\hat{H}$ and then diagonalizing the matrix to obtain both the energies as the corresponding eigenvalues and the coefficients of the intermediate coupling wavefunctions. The matrix elements of the electrostatic interaction ($\hat{H}_e$) and the spin–orbit interaction ($\hat{H}_{so}$) are presented in the following.

2.3.1. Electrostatic interaction $\hat{H}_e$

The Hamilton operator for the electrostatic interaction is:

$$\hat{H}_e = \frac{e^2}{r_{ij}} \propto \sum_{k=0,2,4,6} \mathrm{C}_i^{(k)}\mathrm{C}_j^{(k)} \tag{12}$$

where the expansion is in terms of the tensor operators $\mathrm{C}_q^{(k)} = \sqrt{4\pi/(2k+1)}Y_{kq}$, which are a function of the spherical harmonics Y_{kq} [12]. The matrix elements of $\hat{H}_e$ in Eq. (11) are then given by [12]:

$$\langle l^N SL|C_i^{(k)}\cdot C_j^{(k)}|l^N S'L'\rangle = \delta_{SS'}\delta_{LL'}(-1)^{4l}(-1)^L(2l+1)^2 \times \sum_{k=0,2,4,6} \begin{pmatrix} l & k & l \\ 0 & 0 & 0 \end{pmatrix}^2 \begin{Bmatrix} l & l & k \\ l & l & L \end{Bmatrix} F_{(k)} \tag{13}$$

which for f-electrons ($l=3$) becomes:

$$\langle 4f^N SL|C_i^{(k)}\cdot C_j^{(k)}|4f^N S'L'\rangle = \delta_{SS'}\delta_{LL'}49(-1)^L \times \sum_{k=0,2,4,6} \begin{pmatrix} 3 & k & 3 \\ 0 & 0 & 0 \end{pmatrix}^2 \begin{Bmatrix} 3 & 3 & k \\ 3 & 3 & L \end{Bmatrix} F_{(k)} \tag{14}$$

In Eq.(14), the $\langle 4f^N SL|$ and $|4f^N S'L'\rangle$ are the two interacting states, and the $F_{(k)}$ are the Slater integrals. The sum is limited to $k=0$, 2, 4 and 6 because for all other k the 3j and/or 6j symbols are zero. It

is important to note that since $\hat{H}_e$ is an electric interaction it cannot act on the spin [32], and therefore the matrix element is zero if $S \neq S'$ and $L \neq L'$, as denoted by the Kronecker $\delta_{SS'}$ and $\delta_{LL'}$, respectively. There are two notations $F_{(k)}$ and $F^{(k)}$ for the Slater integrals commonly found in the literature, and the respective conversions are [12]:

$$F_{(0)} = F^{(0)}$$
$$F_{(2)} = F^{(2)}/225$$
$$F_{(4)} = F^{(4)}/1089$$
$$F_{(6)} = 25F^{(6)}/184041 \quad (15)$$

An additional complication in using Eq. (14) arises for $4f^N$ electron configurations with $3 \leq N \leq 11$. As shown in Section 2.1, for these configurations there are some ^{2S+1}L terms with the same L and S which are distinguished by an additional sequential index τ. This produces off-diagonal matrix elements in Eq. (11). This problem was solved by Nielsen and Koster [26] who have applied the respective classification of states by Racah [21] to Eq. (14) and have conveniently and consistently tabulated all electrostatic matrix elements for all $4f^N$electron configurations in the form [26]:

$$\langle 4f^N SL|\hat{H}_e|4f^N S'L'\rangle = \sum_{k=0}^{3} e_k E^{(k)} \quad (16)$$

In Eq. (16), the e_k are the coefficients tabulated in Ref. [26], and the $E^{(k)}$ parameters relate to the Slater integrals [Eq. (15)] according to [21]:

$$E^{(0)} = F_{(0)} - 10F_{(2)} - 33F_{(4)} - 286F_{(6)}$$
$$E^{(1)} = (70F_{(2)} + 231F_{(4)} + 2002F_{(6)})/9$$
$$E^{(2)} = (F_{(2)} - 3F_{(4)} + 7F_{(6)})/9$$
$$E^{(3)} = (5F_{(2)} + 6F_{(4)} - 91F_{(6)})/3 \quad (17)$$

Given a set of Slater integrals $F_{(2)}$, $F_{(4)}$, $F_{(6)}$, the matrix elements of $\hat{H}_e$ in Eq. (3) can now be readily evaluated by applying Eqs. (16 and 17) and using the electrostatic matrix tables by Nielsen and Koster [26]. Note that the $F_{(0)}$ Slater integral is usually omitted as it simply produces a uniform shift of the energies of all the states of the configuration, which is irrelevant when the energies are reference to the ground-state multiplet of the [Xe]$4f^N$ electron configuration [41].

2.3.2. Spin–orbit interaction $\hat{H}_{so}$

The Hamilton operator for the spin–orbit interaction is:

$$\hat{H}_{so} = \sum_{i=1}^{N} \xi(r_i)(\mathbf{s}_i \cdot \mathbf{l}_i) \quad (18)$$

where r_i is the radial coordinate of the ith electron, $\mathbf{s}_i$ and $\mathbf{l}_i$ are the spin and orbital angular momentum, respectively, and $\xi(r_i) = \left(\hbar^2/m^2c^2r_i\right)\{dU(r_i)/dr_i\}$, where $U(r_i)$ is the central field potential [22]. The spin–orbit interaction is not diagonal in the basis set of L and S used in the L–S coupling scheme, and $\hat{H}_{so}$ will therefore contribute off-diagonal elements to the $\hat{H}$-matrix in Eq. (11). Specifically, $\hat{H}_{so}$ mixes all states that have the same J [25]. The matrix elements of $\hat{H}_{so}$ in Eq.(18) are then given by [12,25,32]:

$$\langle 4f^N SLJ|\hat{H}_{so}|4f^N S'L'J'\rangle = \zeta(-1)^{J+L+S'}\sqrt{l(l+1)(2l+1)} \times \begin{Bmatrix} S & S' & 1 \\ L' & L & J \end{Bmatrix} \langle l^N SL\|\mathrm{V}^{(11)}\|l^N S'L'\rangle \quad (19)$$

where $l=3$ for f-electrons, the reduced matrix element $\langle l^N SL||\mathrm{V}^{(11)}||l^N S'L'\rangle$ is given by Eq. (6), and ζ is the spin–orbit coupling parameter which is a constant for all the states of a given 4f configuration in a given material [22].

2.3.3. Intermediate coupling wavefunctions and 4f energy levels

We are now in a position to calculate the matrix elements of $\hat{H} = \hat{H}_e + \hat{H}_{so}$ in Eq. (11) using Eqs. (16 and 19). In the $|4f^N SLJ\rangle$ basis set, the $\hat{H}$-matrix has off-diagonal elements that arise from mixing of different states with the same J by spin–orbit coupling as well as from mixing of states with the same S and L by electrostatic interaction. This is now merely a tedious computational task, and there is no fundamental obstacle in calculating all energies of all the RE^{3+} 4f states given a set of material-specific $F_{(k)}$ and ζ parameters. Numerical diagonalization of the square symmetric $\hat{H}$-matrix solves this eigenvalue problem [Eq. (11)] and yields the wavefunctions and energies of each $|4f^N SLJ\rangle$ state. Robust matrix diagonalization algorithms such as the Jacobi method can be employed [42]. The matrix diagonalization yields the intermediate coupling wavefunction of each $|4f^N SLJ\rangle'$ multiplet, which is expressed as a linear combination of all other states in the configuration having the same J and being mixed by spin–orbit interaction, *i.e.*

$$|4f^N SLJ\rangle' = \sum_i c_i |4f^N S'L'J\rangle \quad (20)$$

where $\sum c_i^2 = 1$. The prime has been added here to emphasize that the actual $|4f^N SLJ\rangle'$ wavefunction is not the pure $|4f^N SLJ\rangle$ wavefunction anymore. This prime is usually omitted, and one therefore has to be aware that the $^{2S+1}L_J$ multiplet labels do not convey the complete nature of the wavefunction. For example, the pure $^4I_{9/2}$ wavefunction of Er^{3+} ($4f^{11}$) in the absence of spin–orbit coupling ($\zeta=0$) is "degraded" to

$$|^4I_{9/2}\rangle' = -0.4083|^4F_{9/2}\rangle - 0.02023|^4G_{9/2}\rangle + 0.6731|^4I_{9/2}\rangle - 0.3122|^2G(1)_{9/2}\rangle + 0.2521|^2G(2)_{9/2}\rangle - 0.2080|^2H(1)_{9/2}\rangle + 0.4190|^2H(2)_{9/2}\rangle \quad (21)$$

in the actual intermediate coupling case of an Er^{3+}-doped aluminosilicate glass ($F_2=433.258\ cm^{-1}$, $F_4=62.3544\ cm^{-1}$, $F_6=7.33668\ cm^{-1}$, and $\zeta=2376\ cm^{-1}$)[43]. Note in Eq. (21) that the actual $|^4I_{9/2}\rangle'$ wavefunction only retains $(0.6731)^2$, *i.e.* 45.3% of its $|^4I_{9/2}\rangle$ origin as a result of spin–orbit coupling, and all the other $J=9/2$ multiplets of the $4f^{11}$ configuration are admixed to various degrees. In some rare cases this can lead to confusion in the labeling of the multiplets, especially for ions towards the end of the

Table 2
Complete set of wavefunctions and respective energies for LaF_3:Tm^{3+} calculated in the intermediate coupling approximation ($F_{(2)}=445.040\ cm^{-1}$, $F_{(4)}=63.9238\ cm^{-1}$, $F_{(6)}=7.60360\ cm^{-1}$, $\zeta=2636\ cm^{-1}$ [35]). The wavefunction components are sorted in descending magnitude, and the purity indicates the magnitude of the $^{2S+1}L_J$ state that is obtained for $\zeta \to 0$.

No.	$^{2S+1}L_J$ ($\zeta \to 0$)	Intermediate coupling wavefunction	Energy (cm^{-1})	Purity (%)
1	$^3H_6$	$0.9953|^3H_6\rangle + 0.09708|^1I_6\rangle$	0	99.1
2	$^3F_4$	$0.7889|^3F_4\rangle + 0.5497|^1G_4\rangle - 0.2748|^3H_4\rangle$	5184	62.2
3	$^3H_5$	$1.0000|^3H_5\rangle$	8223	100.0
4	$^3H_4$	$0.7548|^3H_4\rangle - 0.5311|^3F_4\rangle - 0.3849|^1G_4\rangle$	12359	57.0
5	$^3F_3$	$1.0000|^3F_3\rangle$	13973	100.0
6	$^3F_2$	$0.8807|^3F_2\rangle - 0.4519|^1D_2\rangle - 0.1419|^3P_2\rangle$	14614	77.6
7	$^1G_4$	$0.7414|^1G_4\rangle + 0.5956|^3H_4\rangle - 0.3092|^3F_4\rangle$	20804	55.0
8	$^1D_2$	$0.6685|^3P_2\rangle + 0.6125|^1D_2\rangle + 0.4220|^3F_2\rangle$	27299	37.5
9	$^1I_6$	$0.9953|^1I_6\rangle - 0.0971|^3H_6\rangle$	33414	99.1
10	$^3P_0$	$0.9743|^1P_0\rangle - 0.2251|^1S_0\rangle$	34267	94.9
11	$^3P_1$	$1.0000|^3P_1\rangle$	35058	100.0
12	$^3P_2$	$0.7301|^3P_2\rangle - 0.6486|^1D_2\rangle - 0.2152|^3F_2\rangle$	37390	53.3
13	$^1S_0$	$0.9743|^1S_0\rangle + 0.2251|^3P_0\rangle$	75906	94.9

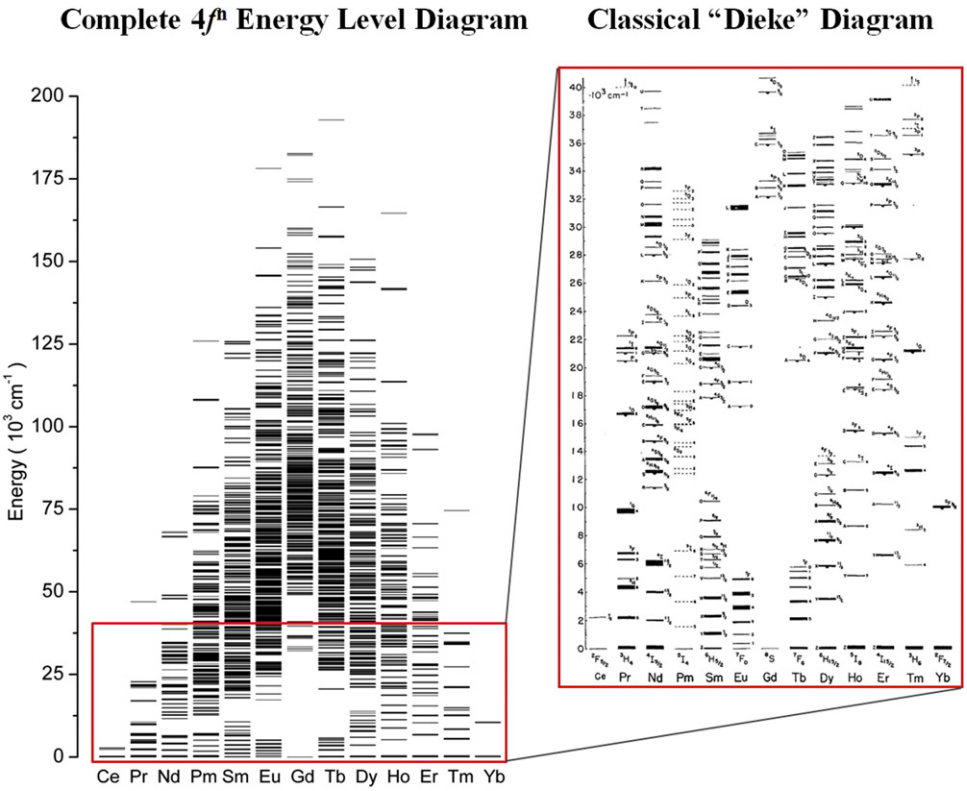

Fig. 4. Energy level diagram for the $^{2S+1}L_J$ multiplets of all RE^{3+} ions. The calculated diagram on the left shows the complete set of $^{2S+1}L_J$ multiplets for each RE^{3+} ion [99]. The classical "Dieke" diagram [65] on the right was compiled in the 1960s from experimental observations. It shows the subset of $^{2S+1}L_J$ multiplets with energies up to 40,000 cm^{-1}, a range that is accessible in a typical optical spectroscopy experiment.

rare-earth series where spin–orbit coupling is strong. Table 2 shows the complete set of intermediate coupling wavefunctions of Tm^{3+} calculated using the parameters for LaF_3:Tm^{3+} [35] as an example for the impact of strong spin–orbit coupling. Inspection of the wavefunction components reveals that not all energy levels can be assigned unambiguously. Two levels, No. 8 at 27299 cm^{-1} and No. 12 at 37390 cm^{-1}, have the $^3P_2$ state as the strongest component, and its contribution amounts to 45% and 53%, respectively. In both cases, the second component of the wavefunction arises from the $^1D_2$ state with the partial weights of 38% and 42%, respectively. Even in spite of such a strong mixture of these states induced by the spin–orbit interaction, the state at 27299 cm^{-1} (No. 8) is labeled as $^1D_2$, whereas its higher energy counterpart is denoted as $^3P_2$. This follows the convention that the $^{2S+1}L_J$ label shall designate the wavefunction that is obtained for $\zeta \rightarrow 0$.

An extensive body of work from the 1950s through the 1970s primarily by G.H. Dieke et al. [41,44–65], W.T. Carnall et al. [35,66–82], and K.H. Hellwege et al. [83–98] has resulted in a comprehensive survey, assignment, and calculation of all $|4f^N SLJ\rangle$ energy levels up to 40,000 cm^{-1}. This seminal body of work is embodied in the famous "Dieke diagram" [65] shown in Fig. 4, which has become the energy level scheme "work horse" used by the community for spectroscopic work with RE^{3+} ions. Fig. 4 also shows a recent calculation of the complete set of $^{2S+1}L_J$ multiplet energies for all RE^{3+} ions [99]. The great utility of the Dieke diagram arises from the fact that the radial extent of the 4f wavefunctions is small compared to the 5s and 5p wavefunctions, *i.e.* the 4f electrons are shielded quite effectively from the effects of the surrounding charges in a solid. This is a unique feature of the rare-earth ions and, as one of its consequences, the $|4f^N SLJ\rangle$ wavefunctions and associated energy levels are rather insensitive to the chemical surroundings of the RE^{3+} ion. This manifests in the spectrally narrow optical transitions and the small crystal-field splittings for RE^{3+} ions in solids. The Dieke diagram therefore provides an excellent first-order energy-level description for a wide range of RE^{3+}-doped materials. We will see below however that for a given RE^{3+} ion, the electrostatic and spin–orbit interactions can vary as much as $\pm 20\%$ from host to host. A careful determination of the respective parameters for a given host-RE^{3+} combination is therefore needed in order to obtain 4f wavefunctions that are of sufficient quality for meaningful energy-level and transition-intensity calculations.

2.3.4. *Optimizing wavefunctions for a RE^{3+}-doped material*

The weak interactions of the RE^{3+} with its surroundings affect both the effective electrostatic and spin–orbit coupling strength to some extent. For a RE^{3+}-doped material there is, therefore, a set of electrostatic ($F_{(2)}$, $F_{(4)}$, $F_{(6)}$) and spin–orbit (ζ) parameters that are characteristic for this RE^{3+} and host material combination. In order to obtain the best $|4f^N SLJ\rangle$ intermediate coupling wavefunctions for a specific RE^{3+}-doped material it is thus necessary to fit these parameters to a set of experimental $^{2S+1}L_J$ multiplet energies. All too often in the literature this step of optimizing electrostatic and spin-orbit parameters is forgotten, not mentioned, or consciously omitted, and wavefunctions and associated reduced matrix elements of *another* material (such as LaF_3:RE^{3+} or aqueous RE^{3+}) are implicitly or sometimes explicitly used from published tables instead. This may result in unphysical Judd–Ofelt intensity parameters.

First, care must be taken in the experimental determination of the $^{2S+1}L_J$ multiplet energies, a deceptively trivial task. The challenge arises from the crystal–field interactions that are present in any real system. These are not included in the Hamiltonian of Eq. (9), and they cause a partial or complete splitting of each $^{2S+1}L_J$ multiplet into its $2J+1$ components, depending on the RE^{3+} ion and

the point symmetry at the RE^{3+} site. The degeneracy-weighted average energy, *i.e.* barycenter energy, of a $^{2S+1}L_J$ multiplet is given by:

$$E_B\left(^{2S+1}L_J\right) = \frac{1}{2J+1}\sum_i g_i E_i \tag{22}$$

where the sum runs over all crystal-field levels with energies E_i of the $^{2S+1}L_J$ multiplet, and g_i is the crystal-field level degeneracy ($\sum g_i = 2J+1$). The $E_B\left(^{2S+1}L_J\right)$ can be determined exactly by first determining the energy and degeneracy of each crystal-field level of each $^{2S+1}L_J$ multiplet using low-temperature polarized absorption and luminescence spectroscopy and then calculating the barycenter energies according to Eq. (22). This approach is laborious and often challenging and therefore well beyond the scope of most studies. It is also not practical for amorphous systems such as RE^{3+}-doped glasses that have significant inhomogeneous broadening, *i.e.* are not characterized by a single set of crystal-field energies. Alternatively, the $E_B\left(^{2S+1}L_J\right)$ can be *approximated* from high-temperature polarized absorption spectra (see Fig. 5). At sufficiently high temperatures, all crystal-field levels of the initial state i are thermally populated and, consequently, all crystal-field transitions from the initial state i to the final state f contribute to the observed absorption spectrum, $\varepsilon(E)$. By assuming equal thermal population of the crystal-field levels in the initial state as well as equal oscillator strength of all crystal-field transitions within the i→f transition, $E_B\left(^{2S+1}L_J\right)$ can be approximated by the energy at which $\int_0^{E_B}\varepsilon(E)dE = 0.5$ in the measured polarization-weighted absorption spectrum. Note that the integral is taken in the energy rather than the wavelength domain in order not to distort the spectral distribution. Determining barycenter energies from high-temperature absorption spectra however has its limitations. Total crystal-field splittings of $^{2S+1}L_J$ ground state multiplets typically range from 200–500 cm^{-1}. While all crystal-field levels of the ground state will be substantially populated at 300 K, their thermal population is far from equal at any practical temperature. As a result, the absorption spectra of transitions to the various excited-state multiplets will be weighted more towards the respective higher-energy crystal-field transitions, and the barycenter energy will be overestimated.

Finally, the electrostatic ($F_{(2)}$, $F_{(4)}$, $F_{(6)}$) and spin–orbit (ζ) parameters can be obtained by fitting calculated barycenter energies to a set of experimental barycenter energies. This is typically done as an unconstrained optimization, and procedures such as the Downhill Simplex algorithm can be used [100]. Here one can choose to either minimize the absolute root-mean-square (RMS) deviation

$$\mathrm{RMS}_{abs} = \sqrt{\frac{1}{n-p}\sum_{i=1}^{n}\left(E_i^{\exp}-E_i^{calc}\right)^2} \tag{23}$$

or the relative RMS deviation

$$\mathrm{RMS}_{rel} = \sqrt{\frac{1}{n-p}\sum_{i=1}^{n}\left(\frac{E_i^{\exp}-E_i^{calc}}{E_i^{\exp}}\right)^2} \tag{24}$$

between the calculated and experimental barycenter energies, where n is the number of experimental barycenter energies and p is the number of fit parameters ($p=4$ in this case) [101]. It is generally preferred to use RMS_{rel} as to not skew the optimization towards the higher-energy multiplets. Similarly, as we will see later, RMS_{rel} is preferably used when fitting the Judd–Ofelt intensity parameters as to not skew the optimization towards the highest-intensity transitions (see Section 3.1.2) [101].

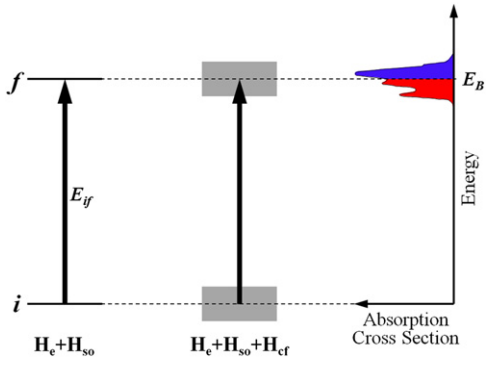

Fig. 5. Determination of the energy (E_{if}) for a measured transition from an initial state (i) to a final state (f). Both states i and f are $(2J+1)$-fold degenerate in the intermediate coupling approximation $\hat{H} = \hat{H}_e + \hat{H}_{so}$ [Eq. (9)]. A real system also has crystal-field interaction $\hat{H}_{cf}$ which lifts some or all of the $(2J+1)$-fold degeneracy and causes each level to split (gray box). The transition energy E_{if} can be approximated by the barycenter energy E_B, at which the integrated absorption cross sections of the low-energy side ($E < E_B$, shown red) and of the high-energy side ($E > E_B$, shown blue) are equal (see Section 2.3.4). (For interpretation of the references to color in this figure legend, the reader is referred to the web version of this article.)

2.3.5. Review of electrostatic and spin–orbit interaction parameters

A great number of studies have been performed over the past decades aimed at modeling the RE^{3+} energy levels doped into various host materials. Some of the studies used the simple Hamilton operator shown in Eq. (9), while more sophisticated studies included a variety of additional higher-order atomic as well as crystal-field interactions. Fig. 6 shows the electrostatic ($F_{(2)}$, $F_{(4)}$, $F_{(6)}$) and spin–orbit (ζ) interaction parameters for 182 RE^{3+}-doped compounds compiled from the literature [13,14,33–39,51–57,62,71,73–75,94,102–147]. One can see that all these parameters increase with an increasing number of 4f electrons. This is due to (1) the enhanced Coulomb repulsion between 4f electrons when moving from Ce to Yb and (2) the increasing atomic number Z, since the spin–orbit interaction is proportional to Z^4 [22]. Recently, Tanner and Duan have given a comprehensive analysis of the crystal-field and free-ion parameters for the entire series of rare-earth ions doped into $Cs_2NaLnCl_6$, and they presented linear and quadratic fits of the electrostatic ($F_{(2)}$, $F_{(4)}$, $F_{(6)}$) and spin–orbit (ζ) interaction parameters as a function of the number of 4f electrons [148]. While there are clear trends for each of the parameters along the RE^{3+} series, the variation of the parameters for a given RE^{3+} ion for different host materials is striking. The electrostatic parameters in particular vary as much as ±20% about their average depending on the chemical environment the RE^{3+} ion is placed in. From Fig. 6 it is readily apparent that using a set of $F_{(2)}$, $F_{(4)}$, $F_{(6)}$ and ζ parameters for a RE^{3+} ion in *one* host to describe the wavefunctions of that RE^{3+} in *another* host can potentially be a poor choice. For example, consider using the atomic parameters for LaF_3:Er^{3+} in an attempt to describe the $\langle {}^4I_{15/2}||U^{(2)}||{}^2H(2)_{11/2}\rangle$ intermediate coupling reduced matrix element in Y_2O_2S:Er^{3+} (see Section 2.4):

LaF_3:Er^{3+}: $F_2 = 445.01\ cm^{-1}$, $F_4 = 68.140\ cm^{-1}$, $F_6 = 7.5269\ cm^{-1}$, $\zeta = 2380\ cm^{-1}$ [137]

$$|\langle {}^4I_{15/2}||U^{(2)}||{}^2H(2)_{11/2}\rangle|^2 = 0.699872$$

Y_2O_2S:Er^{3+}: $F_2 = 429.52\ cm^{-1}$, $F_4 = 64.293\ cm^{-1}$, $F_6 = 6.5218\ cm^{-1}$, $\zeta = 2339\ cm^{-1}$ [141]

$$|\langle {}^4I_{15/2}||U^{(2)}||{}^2H(2)_{11/2}\rangle|^2 = 0.595564$$

The use of LaF_3:Er^{3+} parameters to describe Y_2O_2S:Er^{3+} would overestimate the above squared reduced matrix elements by 17.5%, an error that would directly propagate into the Judd–Ofelt intensity parameters (see Section 3). This illustration further stresses the need to have good wavefunctions for a system at hand *before* performing a Judd–Ofelt intensity calculation.

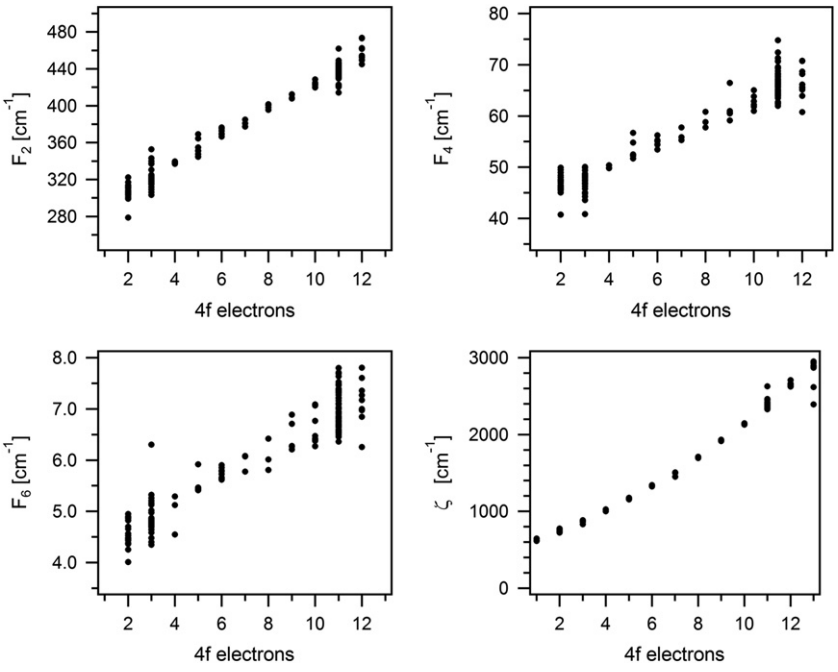

Fig. 6. Electrostatic ($F_{(2)}$, $F_{(4)}$, $F_{(6)}$) and spin–orbit (ζ) interaction parameters for 182 RE^{3+}-doped compounds compiled from the literature (see Section 2.3.5 for references). The studies included here performed a least-squares fit of a Hamiltonian including the electrostatic and spin–orbit interactions, and in many cases also higher-order atomic and crystal-field interactions, to a set of experimental $^{2S+1}L_J$ energies.

2.4. Intermediate coupling reduced matrix elements

Recall that the reduced matrix elements of the various tensor operators described in Section 2.3 were calculated in the context of the pure $|4f^N SLJ\rangle$ wavefunctions, *i.e.* in the absence of spin–orbit interaction. They now need to be evaluated in the intermediate coupling approximation for a specific RE^{3+}-doped material using the wavefunctions obtained in Section 2.3. Fitting of the barycenter energies to a set of experimental $^{2S+1}L_J$ multiplet energies (Section 2.3.4) yields optimized electrostatic ($F_{(2)}$, $F_{(4)}$, $F_{(6)}$) and spin–orbit (ζ) parameters as well as the coefficients c_i of the intermediate coupling wavefunctions [Eq. (20)] (Section 2.3.3). The reduced matrix element of a tensor operator X between two intermediate coupling wavefunctions $|4f^N SLJ\rangle'$ and $|4f^N S'L'J'\rangle'$ is then given by

$$\langle l^N SLJ\|X\|l^N S'L'J'\rangle' = \sum_i \sum_j c_i c_j \langle l^N SLJ\|X\|l^N S'L'J'\rangle \tag{25}$$

where the double sum runs over the i and j components of the two intermediate coupling wavefunctions [Eq.(20)], and the reduced matrix element $\langle l^N SLJ\|X\|l^N S'L'J'\rangle$ is any of Eqs. (5)–(8). Extensive table works of intermediate coupling reduced matrix elements have been published by W.T. Carnall, H. Crosswhite, and H.M. Crosswhite in 1978 for the RE^{3+} ions from Pr^{3+} to Er^{3+} doped into LaF_3 [72]. These tables have found widespread use over the past three decades, and these reduced matrix elements have been used for many RE^{3+}-doped materials besides the LaF_3:RE^{3+} for which they were originally derived. This was due to the rather significant amount of calculations involved in the evaluation of these reduced matrix elements as well as the assumption that the reduced matrix elements would depend little on the nature of the host material. The latter can be a poor approximation if quantitative answers are sought from an energy-level or transition-intensity calculation. With present day computing power this simplification is not necessary, and intermediate coupling matrix elements can be readily calculated for any material following the formalism outlined in the preceding sections.

3. Transitions between 4f electronic states: the Judd–Ofelt theory

3.1. The original Judd–Ofelt theory

3.1.1. Intensities of transitions between 4f electronic states

The probability for a transition from Ψ_1 to Ψ_2 to take place is proportional to the transition moment

$$\vec{M}_{12} = \int \Psi_2 \vec{\mu} \Psi_1 d\tau \tag{26}$$

where $\vec{\mu}$ denotes the dipole moment operator. The integral in Eq. (26) is non-zero only if the direct product of $\Psi_2 \otimes \vec{\mu} \otimes \Psi_1$ is symmetric (*gerade*) with respect to the center of symmetry (also known as Laporte selection rule). The exchange of energy between an electromagnetic field and the electrons of an atom is generally dominated by electric-dipole (ED) interactions, and the electric-dipole operator has *ungerade* (u) inversion symmetry. Likewise, the 4f wavefunctions have *ungerade* (u) inversion symmetry. Hence, for an ED-induced $4f \leftrightarrow 4f$ transition, the direct product is $u \otimes u \otimes u = u$, and the transition has zero probability because the integral in Eq. (26) vanishes.

In order for ED-induced $4f \leftrightarrow 4f$ transitions to occur at all, some admixture of states with opposite, *i.e. gerade*, parity into the 4f wavefunctions is required. In a solid, such admixtures can be mediated by odd-parity crystal-field components (giving rise to electronic transitions) as well as odd-parity vibrations (giving rise to vibronic transitions) [32]. This is the fundamental premise of the Judd–Ofelt theory. The formalism begins by admixing even-parity states φ_{nl} into the pure 4f wavefunction $|f^N JM_J\rangle$ (Section 2) via an odd-parity crystal field in order to obtain a new wavefunction $|B\rangle$,

$$|B\rangle = |f^N JM_J\rangle + \sum_{\varphi_{nl}} \frac{\left\langle \left(\left\langle f^N JM_J \middle| V \middle| \varphi_{nl} \right\rangle \right) \middle| \varphi_{nl} \right\rangle}{E\left(f^N JM_J\right) - E(\varphi_{nl})} \tag{27}$$

where $E(f^N JM_J) - E(\varphi_{nl})$ are the energy differences between the 4f state and the several perturbing even-parity states φ_{nl}, and V is the crystal-field interaction operator. The $4f^{N-1}5d$ states are the even-

parity states that are most strongly admixed into the 4f states because they are closest in energy to the 4f states. The separation between the barycenter energies of the 4f and $4f^{N-1}5d$ states ranges from $\sim$50,000 cm^{-1} for Ce^{3+} to $\sim$100,000 cm^{-1} for Yb^{3+}, while other even-parity states such as $4f^{N-1}6s$ and $4f^{N-1}6d$ are at much higher energies [65]. For the divalent rare-earth ions (RE^{2+}), the $4f^N$–$4f^{N-1}5d$ separation is much smaller than for RE^{3+} ions [32], and the respective $4f^N \rightarrow 4f^{N-1}5d$ transitions can extend into the visible spectral region. These transitions are parity allowed and thus orders of magnitude stronger than $4f^N \rightarrow 4f^N$ transitions; as a result, they tend to mask the weak $4f^N \rightarrow 4f^N$ transitions. Furthermore, the much smaller $4f^N - 4f^{N-1}5d$ energy separation largely invalidates the use of the perturbation approach in Eq. (27). For these reasons, the Judd–Ofelt theory is ill suited to describe $4f^N \rightarrow 4f^N$ transition intensities in RE^{2+} ions.

For a transition between two 4f states $B \rightarrow B'$ and using the admixed wavefunctions of Eq. (27), the matrix element of the electric dipole moment is given by [1],

$$\langle B|D_q^{(k)}|B'\rangle = \sum_{\varphi_{nl}} \left\{ \frac{\langle f^N J M_J|V|\varphi_{nl}\rangle \langle f^N J' M_J'|D_q^{(k)}|\varphi_{nl}\rangle}{E\left(f^N J M_J\right) - E(\varphi_{nl})} + \frac{\langle f^N J' M_J'|V|\varphi_{nl}\rangle \langle f^N J M_J|D_q^{(k)}|\varphi_{nl}\rangle}{E\left(f^N J' M_J'\right) - E(\varphi_{nl})} \right\} \quad (28)$$

Two assumptions are now made in order to solve Eq. (28). First it is assumed that all sublevels of a given even-parity state φ_{nl} are degenerate. This is a rather drastic assumption when compared to typical $4f^N - 4f^{N-1}5d$ separations, because actual crystal-field splittings of the $4f^{N-1}5d$ states for example are on the order of 5000–30,000 cm^{-1} [149]. Second, it is assumed that $E\left(f^N J M_J\right) - E(\varphi_{nl}) = E\left(f^N J' M_J'\right) - E(\varphi_{nl})$. Likewise, this is a rough assumption because the $4f^N - 4f^{N-1}5d$ separation is within a factor of 2–10 of typical $4f \leftrightarrow 4f$ transition energies [41,104]. With these assumptions, however, it is possible to combine the two sums in Eq. (28) and to simplify the matrix element of the electric-dipole moment to a sum of only three terms. Expressed as oscillator strength, the intensity of the ED-induced absorption $|l^N SLJ\rangle \rightarrow |l^N S'L'J'\rangle$ then becomes [1,11,150]

$$f_{ED}^{abs} = \frac{8\pi^2 m_e}{3h} \frac{\nu}{(2J+1)} \frac{\chi_{ED}^{abs}}{n} \sum_{\lambda=2,4,6} \Omega_{(\lambda)} |\langle l^N SLJ||U^{(\lambda)}||l^N S'L'J'\rangle|^2 \quad (29)$$

where $\Omega_{(\lambda)}$ are the three Judd–Ofelt intensity parameters, the reduced matrix element is given by Eq. (5), ν is the mean transition frequency, n is the refractive index at the transition frequency, χ_{ED}^{abs} is the local-field correction, and the summation is over the even-rank reduced matrix elements $\lambda = 2, 4, 6$ of the $U^{(\lambda)}$ tensor operator [151]. The fact that the transition strength can be expanded as the sum of three even-ranked tensors is one of the key results of the work of Judd and Ofelt [151]. The oscillator strength for a magnetic-dipole (MD) induced absorption $|l^N SLJ\rangle \rightarrow |l^N SLJ'\rangle$ only depends on one reduced matrix element $\langle l^N SLJ||L+gS||l^N SLJ'\rangle$. Unlike ED-transitions, it has no intensity scaling parameter and is given by [152]

$$f_{MD}^{abs} = \frac{h\nu}{6m_e c^2} \frac{n}{(2J+1)} \left|\langle l^N SLJ\|L+gS\|l^N SLJ'\rangle\right|^2 \quad (30)$$

where the reduced matrix element is calculated from Eqs. (7) and (8). There is no need for a local-field correction for magnetic fields in non-magnetic materials, *i.e.* $H_{loc}/H = 1$ [153]. Some transitions have both ED and MD contributions, and the total oscillator strength is then given by $f^{abs} = f_{ED}^{abs} + f_{MD}^{abs}$.

The factor χ in Eq.(29) takes into account that the local electric field, E_{loc}, at the site of the ion undergoing an optical transition is generally different from the macroscopic field in the medium, E. Several models for this "local-field correction" have been proposed in the past [154]. The virtual-cavity model (also called Lorentz model) is a reasonable approximation for RE^{3+} ions doped into a solid such as a crystal or glass, while other models have been proposed for nano-particles embedded in a medium [154]. The local-field correction for an ED-induced absorption is given by $\chi_{ED}^{abs} = [E_{loc}/E]^2 = [(n^2+2)/3]^2$ in the virtual-cavity model, which also shows that the oscillator strength is proportional to the square of the electric field. The additional factor of $1/n$ in Eq. (29) is often combined with χ_{ED}^{abs} even though it has a different physical origin. Specifically, the photon flux in vacuum is $\Phi_0 = (c^2/4\pi)E_0^2$ while in a dielectric medium it is $\Phi_m = (\nu/4\pi)n^2E_0^2 = n(c/4\pi)E_0^2$ with $\nu = c/n$. Since the photon flux does not change upon entering the dielectric medium from the vacuum, an additional factor of $1/n$ has to be included in the expression of the ED oscillator strength in Eq. (29) so that $\Phi_0 = \Phi_m$ [16]. Note that the virtual cavity model is strictly only valid for cubic symmetry and for equal polarizability of the RE^{3+} ion and the medium [155,156]. Deviations from this ideal case would require more complex descriptions of the local electric field [156]. In some systems, the empty-cavity model with $\chi_{ED}^{abs} = [E_{loc}/E]^2 = [3n^2/(2n^2+1)]^2$ was found to provide a better description [157,158]. Most studies however implicitly use the virtual-cavity model and the associated local-field correction shown above.

Another complication is the refractive index dispersion of the material. It is often ignored, and a fixed refractive index, *e.g.* the index n_D at the sodium D-line (589.3 nm), is used independent of the wavelength of the transition. This can be problematic for transitions near the band gap energy of the material where the refractive index can easily be up to 30% greater than n_D. It is desirable to include dispersion for example by describing the refractive index with the Sellmeier equation [159]

$$n(\lambda)^2 = 1 + \sum_{i=1}^{3} \frac{B_i \lambda^2}{\lambda^2 - C_i} \quad (31)$$

where B_i and C_i are phenomenological material constants that are typically obtained from a fit of Eq.(31) to a number of refractive index measurements at different wavelengths. The situation is further complicated in anisotropic crystals that have more than one characteristic refractive index. In uniaxial crystals, taking the average of the ordinary and extraordinary refractive index is a good approximation as long as the birefringence is not too large [16]. Finally note that the above ED and MD-induced absorption oscillator strengths have to be multiplied by n^2 for the case of emission [16].

3.1.2. Application to experimental data

We are now in a position to calculate reduced matrix elements with a given set of electrostatic ($F_{(2)}$, $F_{(4)}$, $F_{(6)}$) and spin–orbit (ζ) parameters (see Section 2) and use them to calculate ED and MD oscillator strengths with a given set of three $\Omega_{(\lambda)}$ ($\lambda = 2, 4, 6$) Judd–Ofelt intensity parameters in Eqs. (29 and 30). The calculated total oscillator strengths can then be compared to experimental oscillator strengths as part of the procedure for fitting the $\Omega_{(\lambda)}$ parameters. Experimental oscillator strengths are typically determined from absorption spectra and are calculated according to [16,160]

$$f_{exp} = \frac{4\varepsilon_0 m_e c^2}{e^2} \frac{10\ln(10)}{N_A} \int \varepsilon(\bar{\nu}) d\bar{\nu} = 4.319 \times 10^{-9} \frac{\text{mol}\cdot\text{cm}^2}{\text{l}} \int \varepsilon(\bar{\nu}) d\bar{\nu} \quad (32)$$

where the vacuum permittivity (ε_0), the electron mass (m_e), the speed of light (c), the elementary charge (e), and Avocadro's

number (N_A) are given in SI units, the molar extinction coefficient $\varepsilon(\bar{\nu})$ is given in units of l/(mol cm), and the energy $\bar{\nu}$ is given in units of 1/cm. That is, the integral in Eq. (32) is determined by integrating over the respective band in an absorption spectrum plotted as $\varepsilon(\bar{\nu})$ [l/(mol cm)] as a function of $\bar{\nu}$ [1/cm]. Belaboring the exact units here has some merit because there are different formulae in the literature. The confusion is usually rooted in the definition of the elementary charge, which some authors take as the SI unit 1.60218×10^{-19} C (as is done here) and others as $e^2/\sqrt{4\pi\varepsilon_0}=4.8032\times10^{-10}$ in esu units. Furthermore note that for crystals with symmetries lower than cubic it is necessary to measure polarized absorption spectra and take the appropriate sum to obtain the "unpolarized" $\varepsilon(\bar{\nu})$ for use in Eq. (32). For example, tetragonal, hexagonal, and trigonal crystal systems are typically uniaxial, *i.e.* having an extraordinary axis $\vec{c}$ that is different from the other axes $\vec{a}$. In this case, the "unpolarized" $\varepsilon(\bar{\nu})$ is obtained by separately measuring the σ-polarized $\left(\vec{E}\perp\vec{c}\right)$ and π-polarized $\left(\vec{E}\parallel\vec{c}\right)$ absorption spectra and adding them according to $\varepsilon(\bar{\nu})=2\varepsilon_\sigma(\bar{\nu})+\varepsilon_\pi(\bar{\nu})$ [102]. Unless the material is amorphous or of cubic symmetry, it is therefore critically important to measure all applicable polarizations separately and to properly add them to obtain the "unpolarized" absorption spectrum. Not doing so can introduce substantial errors in the oscillator strengths.

As with fitting the barycenter energies (see Section 2.3.4), a choice must be made here as to which quantity to minimize when fitting the three $\Omega_{(\lambda)}$ Judd–Ofelt intensity parameters to experimental oscillator strengths. In analogy, one can either minimize the absolute root-mean-square (RMS) deviation

$$\mathrm{RMS}_{abs}=\sqrt{\frac{1}{n-p}\sum_{i=1}^{n}\left(f_i^{\exp}-f_i^{calc}\right)^2} \tag{33}$$

or the relative RMS deviation

$$\mathrm{RMS}_{rel}=\sqrt{\frac{1}{n-p}\sum_{i=1}^{n}\left(\frac{f_i^{\exp}-f_i^{calc}}{f_i^{\exp}}\right)^2} \tag{34}$$

between the calculated and experimental oscillator strengths, where n is the number of experimental oscillator strengths and p is the number of fit parameters ($p=3$ in this case). Judd has pointed out that weak transitions contain as much information about the wavefunctions as the strong ones [3], and that this is only properly accounted for by minimizing RMS_{rel} in the fitting procedure. Goldner *et al.* have used both absolute and relative RMS in the analysis of the spectra of a Pr^{3+}-doped fluorozirconate glass, and they have found that only the RMS_{rel} gave stable and physically meaningful values of the $\Omega_{(\lambda)}$ parameters [101] [161]. In particular, they were able to successfully predict the oscillator strength of the $^3H_4\rightarrow{}^3P_2$ transition, which is notoriously difficult to model when fitting with RMS_{abs}.

3.2. Modified Judd–Ofelt theories

The original Judd–Ofelt theory presented in Section 3.1 has been found to provide quantitatively good predictions of the transition strengths of many rare-earth ions in a wide variety of host materials. One prominent exception is Pr^{3+}, for which large deviations of the calculated oscillator strengths compared to the experimental ones were found [162] [163]. Furthermore, the fit of the Judd–Ofelt intensity parameters for Pr^{3+} has sometimes yielded a negative $\Omega_{(2)}$ parameter [164] [165] [166], which is clearly unphysical as it may imply a negative excited-state lifetime. More specifically, the values of the fitted $\Omega_{(\lambda)}$ parameters were sensitive to the Pr^{3+} transitions that were included in the fit, and the calculation could go particularly awry when the high-energy $^3H_4\rightarrow{}^3P_2$ transition ($\sim$22700 cm^{-1} [72]) was included [160,167]. For Pr^{3+}, the energy of the perturbing 4f5d configuration ($\sim$60000 cm^{-1} [41]) is particularly close to the energy of the 4f states. The assumption of the original Judd–Ofelt theory (see Section 3.1) that the energy difference between the perturbing $4f^{N-1}5d$ states and the $4f^N$ states is constant may therefore not be adequate. Specifically, it may range from $\sim$60000 cm^{-1} for $4f^2\left(^3H_4\right)-4f5d$ to $\sim$37300 cm^{-1} for $4f^2\left(^3P_2\right)-4f5d$. Similar failures of the original Judd–Ofelt theory have been observed for Sm^{3+} [168] and Tb^{3+} [169,170]. Several modifications to the original Judd–Ofelt theory have been proposed with a particular focus on Pr^{3+}.

Auzel *et al.* have shown that the interconfigurational energy difference can be accounted for explicitly if the perturbing configurations are restricted to only $4f^{N-1}5d$, a valid approach given that other even-parity configurations are significantly higher in energy [171]. They expanded Eq. (29) to include $4f^N-4f^{N-1}5d$ energy differences explicitly:

$$f_{ED}^{abs}=\frac{8\pi^2m_e}{3h}\frac{\nu}{(2J+1)}\frac{\chi_{ED}^{abs}}{n}\sum_{\lambda=1,2,3,4,5,6}\left[\frac{1}{E(J)-E(4f5d)}+\frac{(-1)^\lambda}{E(J')-E(4f5d)}\right]^2\times\frac{[E(4f)-E(4f5d)]^2}{4}\Omega_{(\lambda)}\left|\langle l^NSLJ\|U^{(\lambda)}\|l^NS'L'J'\rangle\right|^2 \tag{35}$$

by also introducing odd-ranked $U^{(\lambda)}$ tensors. Goldner *et al.* have found this approach to provide a $\sim$30% improvement in the RMS_{rel} but only when considering the even-ranked tensors $\lambda=2, 4, 6$; the additional inclusion of the odd-ranked tensors $\lambda=1, 3, 5$ yielded unphysical results [101]. This may have been in part due to the only six experimental oscillator strengths available to fit the now six $\Omega_{(\lambda)}$ ($\lambda=1, 2, 3, 4, 5, 6$) intensity parameters. A re-examination of this model for an early series RE^{3+} ion with more experimentally accessible transitions (*e.g.* Nd^{3+}) may be warranted. A similar approach has been taken by Kornienko *et al.* [172] [173], who have used third-order perturbation theory to derive the expression

$$f_{ED}^{abs}=\frac{8\pi^2m_e}{3h}\frac{\nu}{(2J+1)}\frac{\chi_{ED}^{abs}}{n}\sum_{\lambda=2,4,6}\Omega_{(\lambda)}\left|\langle l^NSLJ\|U^{(\lambda)}\|l^NS'L'J'\rangle\right|^2\times\{1+2\alpha[E(J)+E(J')-2E(4f)]\} \tag{36}$$

where the parameter $\alpha=1/\{2[E(4f5d)-E(4f)]\}$. For Pr^{3+}, $\alpha\approx10^{-5}$ cm, but it is usually treated as an additional fit parameter. It can be shown that Eq. (36) follows as a first-order development from Eq. (35) by considering the even terms only [101]. Using Eq. (36) for the analysis of Pr^{3+}-doped fluorozirconate glasses yielded a fitted value of $\alpha\approx2.5\times10^{-5}$ cm, which would imply an energy of the 4f5d configuration of $\sim$30000 cm^{-1} [101], which is clearly too low [41]. In turn fixing α to the more realistic value of 10^{-5} cm provided similar results to using the even-ranked terms in Eq. (35). More recently, a further improvement was achieved for Pr^{3+}-doped double molybdates by inclusion of covalent interactions of some Pr^{3+} multiplets with the ligands [174].

Finally, a somewhat more phenomenological approach has been described by Florez *et al.*, who proposed a combination of even and odd-ranked tensors according to [170]

$$f_{ED}^{abs}=\frac{\bar{\nu}}{(2J+1)}\left\{\sum_{\lambda=2,4,6}\tau_{(\lambda)}\left|\langle l^NSLJ\|U^{(\lambda)}\|l^NS'L'J'\rangle\right|^2+\xi^2\sum_{\lambda=1,3,5}\tau_{(\lambda)}\left|\langle l^N\psi'J'\|U^{(\lambda)}\|l^N\psi J\rangle\right|^2\right\} \tag{37}$$

where $\tau_{(\lambda)}=(8\pi^2mc\chi_{ED}^{abs}/3nh)\Omega_{(\lambda)}$, $\bar{\nu}$ is the transition energy in cm^{-1}, and $\xi=\bar{\nu}/\Delta\bar{E}$, where $\Delta\bar{E}$ is the energy difference between

the $4f^N$ and the $4f^{N-1}5d$ configurations. Apart from the second sum in the bracket, Eq. (37) is equivalent to Eq. (29). Using Eq. (37) for the analysis of the spectra of Tb^{3+}-doped fluoroindate glasses, they found that only the combination $\{\tau_{(2)}, \tau_{(3)}, \tau_{(6)}\}$ resulted in all non-zero parameter values.

Overall, these modified Judd–Ofelt theories attempt to refine some of the drastic assumptions made by the original Judd–Ofelt theory. Some improvement is clearly achieved for the well-known problem cases, however usually at the expense of additional fit parameters and some loss of physical insight. In general, the original Judd–Ofelt theory provides useful results, and the modified theories merit consideration only if the original theory is found to fail.

3.3. Derived quantities

Several important quantities can be calculated once the Judd–Ofelt $\Omega_{(\lambda)}$ intensity parameters are known for a specific material system. For example, the rate of spontaneous radiative decay $A^{ED}_{SLJ\to S'L'J'}$ for an electric-dipole transition $\left|l^N SLJ\right\rangle \to \left|l^N S'L'J'\right\rangle$ is given by

$$A^{ED}_{SLJ\to S'L'J'} = \frac{8\pi h\nu^3}{c^3} B^{ED}_{SLJ\to S'L'J'} \tag{38}$$

Here, the Einstein coefficient is:

$$B^{ED}_{SLJ\to S'L'J'} = \frac{e^2}{4hm_e\varepsilon_0\nu} f^{ED} \tag{39}$$

where the oscillator strength f^{ED} is given by Eq. (29) in the context of the Judd–Ofelt theory. Combining Eqs. (29), (38), and (39) yields:

$$A^{ED}_{SLJ\to S'L'J'} = \frac{16\pi^3 e^2}{3\varepsilon_0 hc^3}\frac{\nu^3}{(2J+1)}\chi^{emi}_{ED}\sum_{\lambda=2,4,6}\Omega_{(\lambda)}\left|\langle l^N SLJ\|\mathrm{U}^{(\lambda)}\|l^N S'L'J'\rangle\right|^2 \tag{40}$$

where the fundamental constants are given in SI units, the transition frequency ν is given in (Hz), and the $\Omega_{(\lambda)}$ intensity parameters are in units of (m^2). As mentioned earlier, care should be taken with the definition of the elementary charge, and it is given as 1.60218×10^{-19} C in SI units here. Further note that the local-field correction in emission differs by a factor of n^2 form that in absorption, *i.e.* $\chi^{emi}_{ED} = n^2\chi^{abs}_{ED}$ (see Section 3.1.1) [16]. In analogy, for a magnetic-dipole transition one uses f^{MD} from Eq. (39) to obtain:

$$A^{MD}_{SLJ\to S'L'J'} = \frac{\pi he^2}{3\varepsilon_0 c^5 m_e^2}\frac{\nu^3}{(2J+1)}n^3\left|\langle l^N SLJ||\mathrm{L}+g\mathrm{S}||l^N SLJ'\rangle\right|^2 \tag{41}$$

The total spontaneous radiative decay rate for a transition $|l^N SLJ\rangle \to |l^N S'L'J'\rangle$ is then given by $A_{SLJ\to S'L'J'} = A^{ED}_{SLJ\to S'L'J'} + A^{MD}_{SLJ\to S'L'J'}$. In most cases, an excited state $\left|l^N SLJ\right\rangle$ can decay to *several* lower-energy final states $|l^N S'L'J'\rangle$, and the *total* radiative decay rate of $|l^N SLJ\rangle$ is simply the sum of the respective radiative rates. The resulting radiative lifetime of the $|l^N SLJ\rangle$ excited state is thus given by

$$\tau^{rad}_{SLJ} = \frac{1}{\sum_{S'L'J'}\left(A^{ED}_{SLJ\to S'L'J'} + A^{MD}_{SLJ\to S'L'J'}\right)} \tag{42}$$

It is important to note that Eq. (42) only captures *radiative* contributions to the decay of $|l^N SLJ\rangle$. There can be additional *non-radiative* decay mechanisms such as multi-phonon relaxation and a variety of energy-transfer processes like cross-relaxation, upconversion, and energy migration. The combined rate of these non-radiative decay processes adds to the radiative decay and gives an overall shorter actual lifetime than the purely radiative lifetime calculated from Eq. (42).

Another important characteristic of a decaying $|l^N SLJ\rangle$ excited state is the so-called branching ratio. It is the relative contribution of one $|l^N SLJ\rangle \to |l^N S'L'J'\rangle$ transition to the total radiative decay rate of the $|l^N SLJ\rangle$ excited state, *i.e.*

$$\beta_{SLJ\to S'L'J'} = \frac{A^{ED}_{SLJ\to S'L'J'} + A^{MD}_{SLJ\to S'L'J'}}{\sum_{S'L'J'}\left(A^{ED}_{SLJ\to S'L'J'} + A^{MD}_{SLJ\to S'L'J'}\right)} \tag{43}$$

The branching ratio is directly accessible in an experiment via the relative intensities of the various emissions from a $\left|l^N SLJ\right\rangle$ excited state in a photoluminescence spectrum. A transition with $\beta > 0.5$ is a potential candidate for laser action for a given transition [175] [176].

3.4. Chemical trends

The 4f transitions gain their intensity via admixture of odd-parity crystal-field components (see Section 3.1.1), *i.e.* their intensity and thus the Judd–Ofelt $\Omega_{(\lambda)}$ intensity parameters should depend on the type and symmetry of the ligands in a given material. Görller–Walrand and Binnemans have provided the so far most complete compilation of Judd–Ofelt $\Omega_{(\lambda)}$ intensity parameters for a wide range of rare-earth doped materials [16]. Attempts have been made in the past to correlate the magnitude of the $\Omega_{(\lambda)}$ intensity parameters with the local coordination type and/or geometry of the RE^{3+} ion. Clear correlations are difficult to establish because the coordinating environment has only a small influence on the well-shielded 4f electrons [16], and the intensities of specific 4f→4f transitions generally varies by a factor of two at most. Possibly even more important, the comparison of $\Omega_{(\lambda)}$ intensity parameters from different studies is limited by potentially different computational approaches, such as fitting the $\Omega_{(\lambda)}$ intensity parameters using optimized wavefunctions for the given material *vs.* using wavefunctions from another material, the types of transitions included in the fit, and the type of RMS error minimized in the fitting procedure.

Nevertheless, some general tendencies have been established (see Ref. [16] for a detailed discussion). The $\Omega_{(2)}$ parameter was found to scale with the degree of covalency in the chemical bonds between the RE^{3+} ion and the coordinating ligands [177] in a number of systems. This trend appears to be particularly pronounced for the oscillator strength of hypersensitive transitions (transitions having $|\Delta S| = 0$, $|\Delta L| \le 2$, and $|\Delta J| \le 2$ [16]), which have a large magnitude of the $\langle l^N SLJ||\mathrm{U}^{(2)}||l^N S'L'J'\rangle$ reduced matrix element and thus the $\Omega_{(2)}$ parameter that is associated with it [1]. A variety of models have been suggested over the years regarding the physical origin of this correlation. Trends in $\Omega_{(\lambda)}$ intensity parameters have been studied extensively for RE^{3+} doped glasses, for which a large compositional space is accessible. The $\Omega_{(6)}$ parameter was found to decrease with increasing rigidity of the matrix, which scales inversely with the vibrational amplitude relative to the RE^{3+}-ligand bond length. The rigidity decreases along the series of mixed crystalline oxides, glasses, viscous solutions, hydrated ions, halide vapors, and complexes with organic ligands [178]. A similar trend was found for $\Omega_{(4)}$ [179]. Other authors have correlated $\Omega_{(4)}$ and $\Omega_{(6)}$ with the overlap of the 4f and 5d orbitals [180], the 6s electron density [181], the ion size of the glass modifier [182], the ligand-field distortion [183], the basicity at the RE^{3+} site [184], the degree of covalency in the RE^{3+}-ligand bond [185] [186], and the ionic packing ratio of the glass host [186]. This variety of explanations illustrates the difficulty in identifying consistent trends across many material systems. More importantly, it clearly highlights the rather phenomenological nature of the Judd–Ofelt theory, which is rooted in its various rather drastic assumptions (see

Section 3.1.1). In most cases, therefore, it is difficult to go much beyond treating the $\Omega_{(\lambda)}$ as phenomenological parameters. It would be valuable to reexamine where possible or remeasure where needed the existing body of spectral information using a consistent experimental and computational formalism that includes proper measurement of polarization-weighted oscillator strengths at room temperature, 4f wavefunctions optimized for each material and the associated reduced matrix elements, dispersion and local-field corrections, and the use of relative RMS errors for the least-squares fitting of atomic and Judd–Ofelt $\Omega_{(\lambda)}$ intensity parameters. While this is a daunting undertaking, it would remove methodological differences that exist among past studies and may yield a much clearer picture of chemical and structural trends in the $\Omega_{(\lambda)}$ intensity parameters.

4. A case study: $LaCl_3:Er^{3+}$

It is instructive to discuss the formalisms presented in Sections 2 and 3 in the context of a specific example. We have chosen Er^{3+}-doped $LaCl_3$ because energy-level and intensity measurements as well as calculations with various degrees of sophistication exist for this system. This makes it possible to compare the merits and pitfalls of each model. $LaCl_3$ crystallizes in the hexagonal space group $P6_3/m$ with the La^{3+} site having C_{3h} point symmetry. Er^{3+} can be doped into $LaCl_3$ up to ~2 mol% without changing the $LaCl_3$ structural parameters. The crystal growth and experimental procedures have been described in detail in Ref. [133].

Let us first look at the barycenter energies. In the present work, we have measured σ and π polarized absorption spectra of a $LaCl_3$:1%Er^{3+} single crystal at 300 K, and we now compare these results with an earlier complete crystal-field analysis of this crystal [133]. The barycenter energy results are summarized in Table 3. First, the "unpolarized" absorption spectrum and individual barycenter energies were obtained from the measured σ and π polarized absorption spectra according to Section 2.3.4. We then performed a first calculation (Case #1 in Table 3) that took the electrostatic ($F_{(2)}$, $F_{(4)}$, $F_{(6)}$) and spin–orbit (ζ) interaction parameters derived for $LaF_3:Er^{3+}$ by Carnall *et al.* [72] and used them to calculate the barycenter energies. The average absolute deviation of this calculation is $6 \pm 179\ cm^{-1}$. A second calculation (Case #2 in Table 3) was then performed that fitted the electrostatic ($F_{(2)}$, $F_{(4)}$, $F_{(6)}$) and spin–orbit (ζ) interaction parameters to minimize the relative RMS deviation [Eq. (24)] between the calculated and experimental barycenter energies. This calculation used the respective parameter values of $LaF_3:Er^{3+}$ [72] as starting values for the fit and achieved an average absolute deviation of $42 \pm 101\ cm^{-1}$. The fitting of the atomic parameters for this specific case changed their value by a few percent and decreased the standard deviation by 77%. The energy-level description with the fitted atomic parameters is therefore better than assuming $LaF_3:Er^{3+}$ atomic parameters and, consequently, the wavefunctions should be of better quality. A third calculation (Case #3 in Table 3) was taken from a full crystal-field analysis of $LaCl_3$:1%Er^{3+} [133]. In this work, the barycenter energies are exact because all crystal-field levels are known. This earlier study used a Hamiltonian with 15 atomic and 5 crystal-field parameters to fit 73 experimental crystal-field energies, and it achieved an average absolute deviation of $6.0 \pm 6.8\ cm^{-1}$, *i.e.* about one order of magnitude improvement over Case #2. Table 4 compares the barycenter energies obtained from the 300 K polarized absorption spectra using the $\int_0^{E_B} \varepsilon(E)dE = 0.5$ method (see Section 2.3.4) with the exact barycenter energies from Ref. [133]. The 300 K barycenter energies are found to be overestimated by an average of $39 \pm 33\ cm^{-1}$. One factor contributing to this difference is the unequal thermal population of the crystal-field levels of the $^4I_{15/2}$ ground state multiplet at 300 K (see Section 2.3.4), which are at 0, 36, 63, 95, 112, 140, 179, and $228\ cm^{-1}$ [133]. The thermally weighted average energy of the $^4I_{15/2}$ multiplet is $84.1\ cm^{-1}$ at 300 K and $106.6\ cm^{-1}$ for infinite temperature (equal thermal population), a difference of $22.5\ cm^{-1}$ that contributes to the above overestimate. Another source of deviation arises from the fact that not all individual crystal-field transitions from the $^4I_{15/2}$ multiplet to the various excited-state multiplets have the same oscillator strength. This can cause additional barycenter energy shifts in either direction.

Let us now look at the oscillator strengths (see Table 5). The experimental oscillator strengths were determined from σ and π polarized room-temperature absorption spectra according to $f_{avg} = 2f_\sigma + f_\pi$ [102]. We then calculated intermediate coupling

Table 3

Case study of calculated (E_B^{calc}) *versus* experimental (E_B^{exp}) barycenter energies in $LaCl_3$:1%Er^{3+}. Case #1 took $F_{(k)}$ and ζ parameters derived for $LaF_3:Er^{3+}$ ($F_{(2)}=436.46\ cm^{-1}$, $F_{(4)}=63.995\ cm^{-1}$, $F_{(6)}=6.6679\ cm^{-1}$, $\zeta=2370.0\ cm^{-1}$ [72]) to calculate barycenter energies for $LaCl_3$:1%Er^{3+} in the intermediate coupling approximation [Eq. (9)] using the formalism described in Section 2. Case #2 (present work) used the same formalism but performed a least-squares fit of RMS_{rel} [Eq. (24)] to experimental barycenter energies of $LaCl_3$:1%Er^{3+} determined from polarized room-temperature absorption spectra (see Section 2.3.4) to find optimum $F_{(k)}$ and ζ parameters ($F_{(2)}=433.22\ cm^{-1}$, $F_{(4)}=66.887\ cm^{-1}$, $F_{(6)}=7.2952\ cm^{-1}$, $\zeta=2385.9\ cm^{-1}$). Case #3 is an earlier detailed analysis of $LaCl_3$:1%Er^{3+} that included 15 atomic and 5 crystal-field parameters to fit 73 experimental crystal-field energies [133]. Note that the experimental barycenter energies determined from Case #3 are exact. The quality of the calculation improves considerably from Case #1 to Case #2 to Case #3.

$^{2S+1}L_J$	Case #1			Case #2			Case #3		
	$LaF_3:Er^{3+}$ parameters [72]			This work (300 K)			Full crystal-field analysis [133]		
	E_B^{exp}	E_B^{calc}	$\Delta_{calc-exp}$	E_B^{exp}	E_B^{calc}	$\Delta_{calc-exp}$	E_B^{exp}	E_B^{calc}	$\Delta_{calc-exp}$
$^4I_{15/2}$	0	0		0	0		0	0	
$^4I_{13/2}$	6520	6491	−29	6520	6527	7	6482	6494	12
$^4I_{11/2}$	10165	10001	−164	10165	10145	−20	10112	10116	4
$^4I_{9/2}$	12375	12103	−272	12375	12296	−79	12351	12346	−5
$^4F_{9/2}$	15172	15296	124	15172	15139	−33	15176	15194	18
$^4S_{3/2}$	18383	18495	112	18383	18311	−72	18290	18295	5
$^2H(2)_{11/2}$	19068	19018	−50	19068	19185	117	19035	19046	11
$^4F_{7/2}$	20414	20586	172	20414	20304	−110	20407	20406	-1
$^4F_{5/2}$	22099	22193	94	22099	21949	−150	22065	22068	3
$^4F_{3/2}$	22510	22501	−9	22510	22303	−207	22407	22411	4
$^2G(1)_{9/2}$	24467	24169	−298	24467	24430	−37	24453	24466	13
$^4G_{11/2}$	26290	26540	250	26290	26415	125	26257	26259	2
$\overline{\Delta}_{calc-exp}$			6 ± 179			42 ± 101			6.0 ± 6.8

reduced matrix elements of the $U^{(\lambda)}$ and $L+gS$ tensors (see Section 2.4) using the optimized wavefunctions found above (Case #2 in Table 3) and performed an oscillator-strength analysis using the Judd–Ofelt theory (see Section 3). The calculation also included the refractive index dispersion in the form of the Sellmeier equation [Eq. (31)] and respective parameters derived from Ref. [187]. The least-squares intensity fit minimized the RMS_{rel} [Eq. (34)] and yielded the optimized Judd–Ofelt parameters $\Omega_{(2)} = 5.449 \times 10^{-20}$ cm^2, $\Omega_{(4)} = 2.077 \times 10^{-20}$ cm^2, and $\Omega_{(6)} = 6.873 \times 10^{-21}$ cm^2. The resulting calculated oscillator strengths compare well with experiment and have an average relative deviation of 1.004 ± 0.129. The same Judd–Ofelt analysis was performed, but this time the wavefunctions and respective reduced matrix elements for LaF_3:Er^{3+} were used (Case #1 in Table 3). This calculation yields an average relative deviation of 0.999 ± 0.149. Comparing the two calculations we find that there is a slight improvement of ~10% in the standard deviation by using optimized wavefunctions. Note that for this case, the substantial improvement in the barycenter energy description by using fitted atomic parameters is not as pronounced in the oscillator strength description. In fact, the LaF_3:Er^{3+} wavefunctions provide a rather good description of the oscillator strengths in $LaCl_3$:Er^{3+}. It would be interesting to see how the two approaches compare for other compounds, particularly those that are chemically quite different from LaF_3:Er^{3+}.

Table 4
Comparison of experimental barycenter energies in $LaCl_3$:1%Er^{3+}. The values in the left column were determined from polarized room-temperature absorption spectra using the $\int_0^{E_B} \varepsilon(E)dE = 0.5$ method (see Section 2.3.4). The values in the right column were determined from a complete crystal-field (CF) analysis of $LaCl_3$:1%Er^{3+} and are exact [133]. The first method overestimates the barycenter energies by $\overline{\Delta}_{300K-CF} = 39 \pm 33$ cm^{-1} on average.

$^{2S+1}L_J$	E_B^{exp}, 300 K	E_B^{exp}, Full CF analysis	Δ300K − CF
$^4I_{15/2}$	0	0	
$^4I_{13/2}$	6520	6482	38
$^4I_{11/2}$	10165	10112	53
$^4I_{9/2}$	12375	12351	24
$^4F_{9/2}$	15172	15176	−4
$^4S_{3/2}$	18383	18290	93
$^2H(2)_{11/2}$	19068	19035	33
$^4F_{7/2}$	20414	20407	7
$^4F_{5/2}$	22099	22065	34
$^4F_{3/2}$	22510	22407	103
$^2G(1)_{9/2}$	24467	24453	14
$^4G_{11/2}$	26290	26257	33
$\overline{\Delta}_{300K-CF}$			39 ± 33

The earlier complete crystal-field analysis of $LaCl_3$:Er^{3+} [133] also provided calculated ED and MD oscillator strengths for all individual crystal-field transitions in both σ and π polarization. This data allows us to test the assumption that the oscillator strength of a multiplet transition is sufficiently well approximated by a measurement at 300 K. Fig. 7 shows the calculated line strengths for selected multiplet transitions in $LaCl_3$:Er^{3+}. They exhibit substantial temperature dependencies up to 200 K as the various crystal-field levels of the $^4I_{15/2}$ ground-state multiplet are being thermally populated and lower-energy crystal-field transitions begin to contribute to the total line strength. For this example of $LaCl_3$:Er^{3+} we find that the oscillator strengths of the various multiplet transitions at 300 K deviate by ~13% on average from the ideal case of equal thermal population of the crystal-field levels of the $^4I_{15/2}$ ground state multiplet. This constitutes a significant source of error that is inherent to the Judd–Ofelt approach. We also note in Fig. 7 that the line strength can either increase or decrease with temperature, depending on the strength of the individual crystal-field transitions that contribute to the respective multiplet transition. Therefore, the effect of non-uniform thermal population of the crystal-field levels of the initial state cannot readily be corrected for unless a complete and laborious crystal-field calculation is carried out.

The radiative lifetimes and branching ratios are a good test of the theory because they involve transitions in emission that were not part of the fitting procedure for the $\Omega_{(\lambda)}$ intensity parameters. Table 6 summarizes the calculated radiative relaxation rates and respective radiative lifetimes for the first 8 excited states of Er^{3+} in $LaCl_3$. The calculation used the optimized wavefunctions (Table 3, Case #2) and optimized Judd–Ofelt intensity parameters ($\Omega_{(2)} = 5.449 \times 10^{-20}$ cm^2, $\Omega_{(4)} = 2.077 \times 10^{-20}$ cm^2, $\Omega_{(6)} = 6.873 \times 10^{-21}$ cm^2; Table 5). Where available, we also list experimental lifetimes that were measured at 300 K by direct excitation of

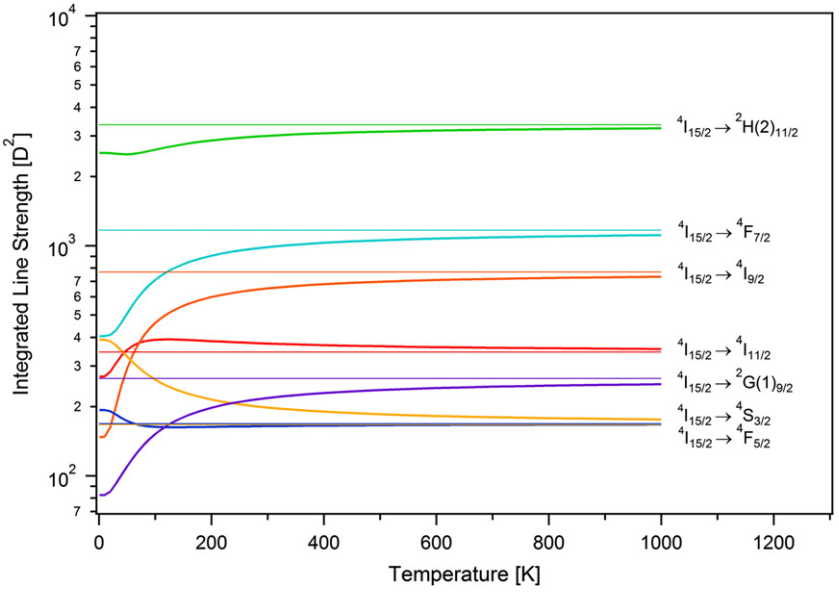

Fig. 7. Calculated total line strengths (in squared Debye units [133]) of selected multiplet transitions in $LaCl_3$:Er^{3+} as a function of temperature (solid bold lines). Also shown are the respective total line strengths for the ideal case of *equal* thermal population of each crystal-field level of the $^4I_{15/2}$ ground-state multiplet (thin horizontal lines).

Table 5
Oscillator strength analysis of $LaCl_3$:1%Er^{3+} using the Judd–Ofelt theory (see Section 3) with calculated reduced matrix elements (see Section 2.4) based on the optimized wavefunctions (Table 3, Case #2). The optimized Judd–Ofelt intensity parameters ($\Omega_{(2)}=5.449\times10^{-20}$ cm^2, $\Omega_{(4)}=2.077\times10^{-20}$ cm^2, $\Omega_{(6)}=6.873\times10^{-21}$ cm^2) were obtained from a least-squares fit of RMS_{rel} [Eq. (34), final $RMS_{rel}=0.2222$] to experimental oscillator strengths determined from σ and π polarized room-temperature absorption spectra according to $f_{avg}=2f_\sigma+f_\pi$ [102]. The refractive index dispersion was assumed to follow the Sellmeier equation [Eq.(31)] with parameters $B_1=0.62646$, $C_1=6.1295\times10^4$ nm^2, $B_2=1.5212$, $C_2=6.1087\times10^3$ nm^2, $B_3=0.2465$, and $C_3=1.4086\times10^4$ nm^{2}derived from Ref. [187]. A calculation (oscillator strengths not shown) using reduced matrix elements calculated from LaF_3:Er^{3+} atomic parameters (Table 3, Case #1) but otherwise identical was also performed and yielded $\Omega_{(2)}=5.575\times10^{-20}$ cm^2, $\Omega_{(4)}=2.258\times10^{-20}$ cm^2, $\Omega_{(6)}=6.430\times10^{-21}$ cm^2 (final $RMS_{rel}=0.2363$). The ratios of calculated and experimental oscillator strengths are shown for both calculations. The last column gives the calculated radiative lifetime of the excited states.

Transition $^4I_{15/2}\rightarrow$	Experimental Oscillator Strengths [10^{-6}]			Calculated Oscillator Strengths [10^{-6}]					τ_{rad}^{calc} (μs)
	f_π^{exp}	f_σ^{exp}	f_{avg}^{exp}	f_{ED}^{calc} Optimized	f_{MD}^{calc} Optimized	f_{total}^{calc} Optimized	$f_{total}^{calc}/f_{avg}^{exp}$ Optimized	$f_{total}^{calc}/f_{avg}^{exp}$ LaF_3:Er^{3+}	Optimized
$^4I_{13/2}$	0.5825	0.5780	1.738	1.039	0.5757	1.615	0.929	0.911	5577
$^4I_{11/2}$	0.1114	0.1948	0.5010	0.5527	0	0.5270	1.052	1.015	4954
$^4I_{9/2}$	0.2212	0.1323	0.4858	0.5733	0	0.5733	1.180	1.090	2735
$^4F_{9/2}$	1.289	0.8767	3.043	2.641	0	2.641	0.868	0.925	403
$^4S_{3/2}$	0.1199	0.1297	0.3794	0.3502	0	0.3502	0.923	0.821	597
$^2H(2)_{11/2}$	2.074	4.404	10.88	11.56	0	11.56	1.062	0.903	67
$^4F_{7/2}$	0.8680	0.7995	2.467	1.897	0	1.897	0.769	0.760	184
$^4F_{5/2}$	0.1070	0.1434	0.3939	0.4348	0	0.4348	1.104	1.031	272
$^4F_{3/2}$	0.07296	0.07003	0.2130	0.2505	0	0.2505	1.176	1.190	333
$^2G(1)_{9/2}$	0.1615	0.2180	0.5976	0.6142	0	0.6142	1.028	1.219	96
$^4G_{11/2}$	4.743	8.967	22.68	21.59	0	21.59	0.952	1.121	16
Average							1.004 ± 0.129	0.999 ± 0.149	

the respective excited state. Multiphonon relaxation generally becomes negligible compared to radiative relaxation if more than 6 phonons are involved in the relaxation to the next lower electronic state. The maximum optical phonon energy of $LaCl_3$ is 263 cm^{-1} [188], and Table 6 shows multiphonon relaxation rates calculated using the parameters for $LaCl_3$ given in Ref. [189]. With the exception of $^4F_{7/2}$ and $^4F_{5/2}$ (the $^2H(2)_{11/2}$ is a special case discussed below), multiphonon relaxation is completely suppressed for all states in Table 6, and radiative relaxation is expected to be the dominant relaxation mechanism. The calculated lifetimes for $^4I_{13/2}$, $^4I_{11/2}$, and $^4F_{9/2}$, while of the correct magnitude, are longer by 10–40% than the measured lifetimes. This may indicate a limitation of the calculation and/or the presence of additional non-radiative processes. Both $^4I_{13/2}$ and $^4I_{11/2}$ can undergo energy-transfer upconversion processes with an excited neighboring Er^{3+} ion, which would shorten the respective lifetimes from their purely radiative values. The $^4S_{3/2}$ excited state is an interesting case because it is located only 745 cm^{-1} below the $^2H(2)_{11/2}$ state. The two states are in thermal equilibrium which couples their radiative decays. At 300 K and by properly taking the $(2J+1)$ multiplet degeneracies into account, the $^2H(2)_{11/2}$ has a thermal population of $p_{11/2}=0.0777$. The expected radiative relaxation rate of the coupled system is then given by the weighted average $p_{3/2}A_{3/2}+p_{11/2}A_{11/2}$, which yields a calculated lifetime of 377 μs that is within 15% of the measured lifetime of 330 μs. The calculation overestimates the $^4F_{5/2}$ lifetime by ~70%. The multiphon relaxation rate, k_{mp}, of this state is calculated to 5037 s^{-1} [189] and therefore competes with radiative relaxation. The combined rate $A_{rad}^{total}+k_{mp}=8726$ s^{-1}, which corresponds to a lifetime of 115 μs that is within 40% of the measured lifetime.

Finally, branching ratios offer another test of the Judd–Ofelt theory. Unfortunately, Er^{3+} poses some experimental challenges for the measurement of branching ratios because the first few excited states are at relatively high energy, and radiative transitions to these final states are located in the infrared region. We have measured a branching ratio of 3.06 for the $^4F_{7/2}\rightarrow{}^4I_{15/2}$, $^4I_{13/2}$ transitions, which is quite close to the value of 3.65 expected from the respective calculated radiative rates in Table 6.

5. Conclusions

The Judd–Ofelt theory has become a centerpiece of rare-earth optical spectroscopy over the past five decades. It has spurred research into the theoretical foundations of the model and led to numerous modifications over the years. In parallel, the theory has been applied to a broad range of rare-earth-doped solids. Many of the studied materials have important applications in solid-state lasers, optical amplifiers, phosphors for displays and solid-state lighting, upconversion and quantum-cutting materials, and fluorescent markers. The Judd–Ofelt theory has proven to be a valuable tool to analyze transition intensities, identify specific transitions of interest, and make estimates of quantum efficiencies. Our attempt in this paper was to provide the experimentalist with a comprehensive toolset that is suited for the calculation of the 4f wavefunctions, the associated energies and reduced matrix elements, and the Judd–Ofelt intensity parameters.

We have reviewed the two main assumptions made by the original Judd–Ofelt theory (Section 3.1.1), *i.e.* (1) all crystal-field levels of the perturbing odd-parity states (primarily $4f^{N-1}5d$) are assumed to be degenerate, and (2) the energy difference between a $4f^N(SLJ)$ multiplet and the degenerate perturbing odd-parity states is assumed to be the same for all $4f^N(SLJ)$ multiplets. These two approximations allowed the transition strength to be expanded as the sum of three even-ranked tensors, which is the key accomplishment of Judd and Ofelt. Various modified Judd–Ofelt theories have partially addressed these assumptions over the years and achieved up to 30% improvements in the accuracy of calculated oscillator strengths (Section 3.2). Nevertheless, it is important to be aware of a number of additional assumptions, limitations, and pitfalls that are typically encountered when applying the Judd–Ofelt theory in practice. Any study using a Judd–Ofelt analysis should explicitly discuss or – at a minimum – state the following six assumptions and conditions:

- The type of *4f wavefunctions* that were used to calculate the reduced matrix elements. Ideally, the 4f wavefunctions are obtained by fitting an intermediate coupling Hamiltonian Eq. (9) to a set of experimental barycenter energies (Section 2.3.4),

Table 6
Calculated ED (A_{rad}^{ED}) and MD (A_{rad}^{MD}) radiative decay rates, total radiative lifetime (τ_{rad}), and branching ratios (β) in $LaCl_3$:Er^{3+}. The calculation used the optimized wavefunctions (Table 3, Case #2) and optimized Judd–Ofelt intensity parameters ($\Omega_{(2)} = 5.449 \times 10^{-20}$ cm^2, $\Omega_{(4)} = 2.077 \times 10^{-20}$ cm^2, $\Omega_{(6)} = 6.873 \times 10^{-21}$ cm^2; Table 5). Where available, the measured lifetime (exp) obtained from direct excitation of the respective excited state is given. Also shown are multiponon relaxation rates, k_{mp}, calculated using the parameters given in Ref. [189].

Transition		A_{rad}^{ED} (s^{-1})	A_{rad}^{MD} (s^{-1})	A_{rad}^{total} (s^{-1})	k_{mp} (s^{-1})	τ_{rad} (μs)	β
$^4I_{13/2}$	$\rightarrow {}^4I_{15/2}$	115.3	63.9	179.2	≈ 0	5580	1.00
				179.2		*5000* (exp)	
$^4I_{11/2}$	$\rightarrow {}^4I_{15/2}$	163.0	0.0	163.0	≈ 0	5035	0.82
	$\rightarrow {}^4I_{13/2}$	21.8	13.9	35.7		*4000* (exp)	0.18
				198.7			
$^4I_{9/2}$	$\rightarrow {}^4I_{15/2}$	319.4	0.0	319.4	1	2735	0.87
	$\rightarrow {}^4I_{13/2}$	43.8	0.0	43.8			0.12
	$\rightarrow {}^4I_{11/2}$	1.0	1.5	2.5			0.01
				365.7			
$^4F_{9/2}$	$\rightarrow {}^4I_{15/2}$	2274.6	0.0	2274.6	≈ 0	403.0	0.92
	$\rightarrow {}^4I_{13/2}$	116.8	0.0	116.8		*280* (exp)	0.05
	$\rightarrow {}^4I_{11/2}$	68.8	10.5	79.3			0.03
	$\rightarrow {}^4I_{9/2}$	7.0	3.9	10.8			0.00
				2481.5			
$^4S_{3/2}$	$\rightarrow {}^4I_{15/2}$	1129.3	0.0	1129.3	≈ 0	593.8	0.67
	$\rightarrow {}^4I_{13/2}$	438.3	0.0	438.3		*330* (exp)	0.26
	$\rightarrow {}^4I_{11/2}$	36.3	0.0	36.3			0.02
	$\rightarrow {}^4I_{9/2}$	79.4	0.0	79.4			0.05
	$\rightarrow {}^4F_{9/2}$	0.7	0.0	0.7			0.00
				1684.0			
$^2H(2)_{11/2}$	$\rightarrow {}^4I_{15/2}$	13121.3	0.0	13121.3		70.8	0.93
	$\rightarrow {}^4I_{13/2}$	216.3	112.6	328.9			0.02
	$\rightarrow {}^4I_{11/2}$	135.3	309.6	444.9			0.03
	$\rightarrow {}^4I_{9/2}$	170.1	4.3	174.4			0.01
	$\rightarrow {}^4F_{9/2}$	45.2	0.3	45.5			0.00
	$\rightarrow {}^4S_{3/2}$	0.1	0.0	0.1			0.00
				14115.1			
$^4F_{7/2}$	$\rightarrow {}^4I_{15/2}$	3805.7	0.0	3805.7	3.01×10^5	183.7	0.70
	$\rightarrow {}^4I_{13/2}$	1041.5	0.0	1041.5			0.19
	$\rightarrow {}^4I_{11/2}$	391.8	0.0	391.8			0.07
	$\rightarrow {}^4I_{9/2}$	163.0	15.6	178.6			0.03
	$\rightarrow {}^4F_{9/2}$	10.6	15.8	26.4			0.01
	$\rightarrow {}^4S_{3/2}$	0.1	0.0	0.1			0.00
	$\rightarrow {}^2H(2)_{11/2}$	0.7	0.0	0.7			0.00
				5444.8			
$^4F_{5/2}$	$\rightarrow {}^4I_{15/2}$	1382.6	0.0	1382.6	5037	271.1	0.38
	$\rightarrow {}^4I_{13/2}$	1714.9	0.0	1714.9		*160* (exp)	0.47
	$\rightarrow {}^4I_{11/2}$	249.7	0.0	249.7			0.07
	$\rightarrow {}^4I_{9/2}$	159.0	0.0	159.0			0.04
	$\rightarrow {}^4F_{9/2}$	173.2	0.0	173.2			0.05
	$\rightarrow {}^4S_{3/2}$	1.7	0.8	2.5			0.00
	$\rightarrow {}^2H(2)_{11/2}$	3.8	0.0	3.8			0.00
	$\rightarrow {}^4F_{7/2}$	1.8	1.3	3.1			0.00
				3688.8			

followed by calculation of the reduced matrix elements using the optimized atomic parameters (Section 2.4).

- The type of model used for describing the *refractive index dispersion*. Depending on the compound, the refractive index can easily be ~30% higher in the near UV compared to the near infrared spectral region (Section 3.1.1). This enters the oscillator strength via the term χ_{ED}^{abs}/n [see Eq. (29)] and can induce errors on the order of 50% in the calculated oscillator strength unless an adequate dispersion description such as the Sellmeier model [Eq. (31)] is used.
- The type of *local-field correction* that was used. A typical choice is the virtual-cavity model (Section 3.1.1) which, however, is strictly only valid for cubic symmetry and for equal polarizability of the RE^{3+} ion and the medium.
- The *temperature* at which absorption spectra were measured. The determination of barycenter energies and oscillator strengths for a Judd–Ofelt analysis assumes equal population of all crystal-field levels of the initial state of a transition (Sections 2.3.4 and 4). While room temperature measurements are usually the practical choice, we have shown that errors in the oscillator strength on the order of 10–15% in either direction are to be expected from a measurement at 300 K.
- The method used to account for *polarization*. The Judd–Ofelt theory is formulated for unpolarized transitions, an assumption that is usually well met for amorphous systems such as glasses and liquids. In crystals with symmetry lower than cubic, however, absorption spectra polarized along the various crystal axes have to be measured individually and then properly averaged. The polarization-weighted molar extinction coefficient is $\varepsilon(\overline{\nu}) = 2\varepsilon_\sigma(\overline{\nu}) + \varepsilon_\pi(\overline{\nu})$ for uniaxial systems (tetragonal, hexagonal and trigonal) (Section 3.1.2). More complex formulations are needed for even lower symmetry crystals.
- The type of *root-mean-square* (*RMS*) *error* that was used in the least-squares optimization of both the 4f wavefunctions and the Judd–Ofelt intensity parameters (Sections 2.3.4 and 3.1.2).

Minimizing the relative RMS error (Eqs. (24 and 34), respectively) makes best use of the available information and typically provides better results than minimizing the absolute RMS error (Eqs. (23 and 33), respectively).

This paper may serve as a useful starting point for research in this area. We hope that the Judd–Ofelt theory continues to evolve and to provide valuable insights in future rare-earth material research.

6. Note

A public and free version of a software package based on the formalism presented here will be available for download from Los Alamos National Laboratory. Please contact the first author for instructions.

Acknowledgments

M.P. Hehlen acknowledges financial support by the Los Alamos National Laboratory LDRD Program (LDRD 20120246ER) and thanks Nathaniel Gustafson and Alison R. Mercer-Smith for their assistance with compiling data for the Judd–Ofelt calculations. M.G. Brik appreciates financial support from the European Union through the European Regional Development Fund (Center of Excellence "Mesosystems: Theory and Applications", TK114).

References

[1] B.R. Judd, Phys. Rev. 127 (1962) 750.
[2] G.S. Ofelt, J. Chem. Phys. 37 (1962) 511.
[3] B.R. Judd, Mol. Phys. 101 (2003) 885.
[4] B.R. Judd, Curr. Contents (1984) 20.
[5] J. Hoogschagen, De Absorptiespectra van de Zeldzame Aarden, Noord-Hollandsche Uitgevers Maatschappij, Amsterdam, 1947.
[6] J. Hoogschagen, C.J. Gorter, Physica 14 (1948) 197.
[7] J.H. van Vleck, J. Phys. Chem. 41 (1937) 67.
[8] J.H. van Vleck, The Theory of Electric and Magnetic Susceptibilities, Oxford University Press, London, 1932.
[9] B.G. Wybourne, J. Chem. Phys. 32 (1960) 639.
[10] B.G. Wybourne, J. Chem. Phys. 34 (1961) 279.
[11] J.D. Axe, J. Chem. Phys. 39 (1963) 1154.
[12] B.R. Judd, Operator Techniques in Atomic Spectroscopy, McGraw-Hill Book Company, New York, 1963.
[13] M.J. Weber, Phys. Rev. 157 (1967) 262.
[14] W.F. Krupke, J.B. Gruber, Phys. Rev. 139 (1965) A2008.
[15] W.F. Krupke, Phys. Rev. 145 (1966) 325.
[16] C. Görller-Walrand, K. Binnemans, Spectral intensities of f–f transitions, in: K.A. Gschneidner Jr., L. Eyring (Eds.), Handbook on the Physics and Chemistry of Rare Earths, 25, North-Holland, Amsterdam, 1998, p. 101.
[17] M.F. Reid, Transition intensities, Crystal Field Handbook, Cambridge University Press, Cambridge, 2000 190p.
[18] J.C. Slater, Phys. Rev. 34 (1929) 1293.
[19] G. Racah, Phys. Rev. 62 (1942) 438.
[20] G. Racah, Phys. Rev. 63 (1943) 367.
[21] G. Racah, Phys. Rev. 76 (1949) 1352.
[22] E.U. Condon, G.H. Shortley, The Theory of Atomic Spectra, The University Press, Cambridge, 1953.
[23] M. Rotenberg, R. Bivens, N. Metropolis, J.K. Wooten Jr, The 3-j and 6-j Symbols, Technology Press, Cambridge, 1959.
[24] E.P. Wigner, Group Theory and Its Application to the Quantum Mechanics of Atomic Spectra, Academic Press, New York, 1959.
[25] B.G. Wybourne, Spectroscopic Properties of Rare Earths, Wiley, New York, 1965.
[26] C.W. Nielsen, G.F. Koster, Spectroscopic Coefficiencts for the p, d, and f Configurations, The MIT Press, Cambridge, 1963.
[27] H.A. Kramers, Proc. R Soc Acad. Amsterdam 33 (1930) 959.
[28] A. Messiah, Clebsch–Gordan coefficients and 3j symbols, Quantum Mechanics, vol. 2, North-Holland, Amsterdam, 1962, pp. 1054–1060.
[29] B.W. Shore, D.H. Menzel, Principles of Atomic Spectra, Wiley, New York, 1968.
[30] A. Messiah, Racah coefficients and 6j symbols, Quantum Mechanics, vol. 2, North-Holland, Amsterdam, 1962, pp. 567–569 and 1061–1066.
[31] C. Eckart, Rev. Mod. Phys. 2 (1930) 305–380.
[32] S. Hüfner, Optical Spectra of Transparent Rare Earth Compounds, Academic Press, New York, 1978.
[33] J.R. Quagliano, N.J. Cockroft, K.E. Gunde, F.S. Richardson, J. Chem. Phys. 105 (1996) 9812.
[34] M.P. Hehlen, H.U. Güdel, J.R. Quagliano, J. Chem. Phys. 101 (1994) 10303.
[35] W.T. Carnall, G.L. Goodman, K. Rajnak, R.S. Rana, J. Chem. Phys. 90 (1989) 3443.
[36] J.B. Gruber, M.E. Hills, T.H. Allik, C.K. Jayasankar, J.R. Quagliano, F.S. Richardson, Phys. Rev. B 41 (1990) 7999.
[37] J.R. Quagliano, F.S. Richardson, M.F. Reid, J. Alloys Compd. 180 (1992) 131.
[38] J.B. Gruber, J.R. Quagliano, M.F. Reid, F.S. Richardson, M.E. Hills, M.D. Seltzer, S.B. Stevens, C.A. Morrison, T.H. Allik, Phys. Rev. B 48 (1993) 15561.
[39] S.R. Lüthi, H.U. Güdel, M.P. Hehlen, J.R. Quagliano, Phys. Rev. B 57 (1998) 15229.
[40] B.R. Judd, Proc. Phys. Soc. London Sect. A 69 (1956) 157.
[41] G.H. Dieke, Spectra and Energy Levels of Rare Earth Ions in Crystals, Interscience Publishers, New York, 1968.
[42] W.H. Press, S.A. Teukolsky, W.T. Vetterling, B.P. Flannery, Numerical Recipes in C, Cambridge University Press, Cambridge, 1988.
[43] G. Lakshminarayana, E.M. Weis, D.J. Williams, M.P. Hehlen, in preparation.
[44] G.H. Dieke, S. Singh, J. Opt. Soc. Am. 46 (1956) 495.
[45] G.H. Dieke, L. Heroux, Phys. Rev. 103 (1956) 1227.
[46] G.H. Dieke, H.M. Crosswhite, J. Opt. Soc. Am. 46 (1956) 885.
[47] S.P. Cook, G.H. Dieke, J. Chem. Phys. 27 (1957) 1213.
[48] G.H. Dieke, L. Leopold, J. Opt. Soc. Am. 47 (1957) 944.
[49] E. Carlson, G.H. Dieke, J. Chem. Phys. 29 (1958) 229.
[50] G.H. Dieke, R. Sarup, J. Chem. Phys. 29 (1958) 741.
[51] F. Varsanyi, G.H. Dieke, J. Chem. Phys. 33 (1960) 1616.
[52] H. Crosswhite, G.H. Dieke, J. Chem. Phys. 35 (1961) 1535.
[53] G.H. Dieke, H.M. Crosswhite, B. Dunn, J. Opt. Soc. Am. 51 (1961) 820.
[54] M.S. Magno, G.H. Dieke, J. Chem. Phys. 37 (1962) 2354.
[55] F. Varsanyi, G.H. Dieke, J. Chem. Phys. 36 (1962) 2951.
[56] F. Varsanyi, G.H. Dieke, J. Chem. Phys. 36 (1962) 835.
[57] J.D. Axe, G.H. Dieke, J. Chem. Phys. 37 (1962) 2364.
[58] L.G. DeShazer, G.H. Dieke, J. Chem. Phys. 38 (1963) 2190.
[59] K.S. Thomas, S. Singh, G.H. Dieke, J. Chem. Phys. 38 (1963) 2180.
[60] G.H. Dieke, B. Pandey, J. Chem. Phys. 41 (1964) 1952.
[61] J.W. Rakestra, G.H. Dieke, J. Chem. Phys. 42 (1965) 873.
[62] H.M. Crosswhite, G.H. Dieke, W.J. Carter, J. Chem. Phys. 43 (1965) 2047.
[63] N.H. Kiess, G.H. Dieke, J. Chem. Phys. 45 (1966) 2729.
[64] A.H. Piksis, G.H. Dieke, H.M. Crosshite, J. Chem. Phys. 47 (1967) 5083.
[65] G.H. Dieke, H.M. Crosswhite, Appl. Optics 2 (1963) 675.
[66] W.T. Carnall, Anal. Chem. 34 (1962) 786.
[67] W.T. Carnall, R.L. McBeth, D.M. Gruen, J. Phys. Chem. 66 (1962) 2159.
[68] W.T. Carnall, J. Phys. Chem. 67 (1963) 1206.
[69] W.T. Carnall, P.R. Fields, G.E. Toogood, J. Phys. Chem. 68 (1964) 2351.
[70] W.T. Carnall, P.R. Fields, Adv. Chem. Ser. (1967) 86.
[71] W.T. Carnall, P.R. Fields, K. Rajnak, J. Chem. Phys. 49 (1968) 4443.
[72] W.T. Carnall, H. Crosswhite, H.M. Crosswhite, Energy level structure and transition probabilities in the spectra of the trivalent lanthanides in LaF_3, Argonne National Laboratory Report no. ANL-78-XX-95, 1978.
[73] W.T. Carnall, P.R. Fields, K. Rajnak, J.Chem. Phys. 49 (1968) 4447.
[74] W.T. Carnall, P.R. Fields, K. Rajnak, J. Chem. Phys. 49 (1968) 4450.
[75] W.T. Carnall, P.R. Fields, K. Rajnak, J. Chem. Phys. 49 (1968) 4424.
[76] H.M. Crosswhite, R.L. Schwieso, W.T. Carnall, J. Chem. Phys. 50 (1969) 5032.
[77] W.T. Carnall, P.R. Fields, R. Sarup, J. Chem. Phys. 51 (1969) 2587.
[78] W.T. Carnall, P.R. Fields, J. Morrison, R. Sarup, J. Chem. Phys. 52 (1970) 4054.
[79] W.T. Carnall, P.R. Fields, R. Sarup, J. Chem. Phys. 54 (1971) 1476.
[80] W.T. Carnall, R. Sarup, P.R. Fields, J. Chem. Phys. 57 (1972) 43.
[81] W.T. Carnall, S. Siegel, J.R. Ferraro, B. Tani, E. Gebert, Inorg. Chem. 12 (1973) 560.
[82] W.T. Carnall, H. Crosswhite, H.M. Crosswhite, J.G. Conway, J. Chem. Phys. 64 (1976) 3582.
[83] K.H. Hellwege, Naturwissenschaften 34 (1947) 225.
[84] A.M. Hellwege, K.H. Hellwege, Z. Phys. 130 (1951) 549.
[85] A. Friederich, K.H. Hellwege, H. Lammermann, Z. Phys. 158 (1960) 251.
[86] K.H. Hellwege, G. Hess, H.G. Kahle, Z. Phys. 159 (1960) 333.
[87] A. Friederich, K.H. Hellwege, H. Lammermann, Z. Phys. 159 (1960) 524.
[88] K.H. Hellwege, S. Hüfner, H.G. Kahle, Z. Phys. 160 (1960) 149.
[89] I. Grohmann, K.H. Hellwege, H.G. Kahle, Z. Phys. 164 (1961) 243.
[90] K.H. Hellwege, H. Lammermann, S. Hüfner, G. Horstik, Z. Phys. 165 (1961) 253.
[91] K.H. Hellwege, S. Hüfner, D. Kuse, Z. Phys. 167 (1962) 258.
[92] K.H. Hellwege, S. Hüfner, A. Pocker, Z. Phys. 172 (1963) 453.
[93] K.H. Hellwege, S. Hüfner, H. Schmidt, Z. Phys. 172 (1963) 460.
[94] K.H. Hellwege, E. Orlich, G. Schaack, Phys. Cond. Mater. 4 (1965) 196.
[95] K.H. Hellwege, S. Hüfner, M. Schinkmann, H. Schmidt, Phys. Cond. Mater. 4 (1966) 397.
[96] P. Grünberg, K.H. Hellwege, S. Hüfner, Phys. Cond. Mater. 6 (1967) 95.
[97] N. Haage, K.H. Hellwege, J. Jäger, G. Schaack, Phys. Cond. Mater. 10 (1969) 144.
[98] J. Heber, K.H. Hellwege, U. Kobler, H. Murmann, Z. Phys. 237 (1970) 189.
[99] P.S. Peijzel, A. Meijerink, R.T. Wegh, M.F. Reid, G.W. Burdick, J. Sol. State Chem. 178 (2005) 448.
[100] J.A. Nelder, R. Mead, Comput. J. 7 (1965) 308.
[101] P. Goldner, F. Auzel, J. Appl. Phys. 79 (1996) 7972.

[102] P.S. May, M.F. Reid, F.S. Richardson, Mol. Phys. 61 (1987) 1455.
[103] M.F. Reid, F.S. Richardson, J. Chem. Phys. 83 (1985) 3831.
[104] M.F. Reid, L. van Pieterson, R.T. Wegh, A. Meijerink, Phys. Rev. B 62 (2000) 14744.
[105] C.K. Jayasankar, F.S. Richardson, M.F. Reid, J. Less-Comm. Met. 148 (1989) 289.
[106] S.J. Lakshman, S. Buddhudu, J. Quant. Spectrosc. Radiat. Transfer 24 (1980) 251.
[107] A. Suresh Kumar, S.J. Lakshman, J. Less-Comm. Met. 148 (1989) 357.
[108] J. Sugar, Phys. Rev. 14 (1965) 731.
[109] R. Sarup, M.H. Crozier, J. Chem. Phys. 42 (1965) 371.
[110] J. Markovsky, W. Low, S. Yatsiv, Phys. Lett. 2 (1962) 186.
[111] M.F. Reid, F.S. Richardson, P.A. Tanner, Mol. Phys. 60 (1987) 881.
[112] R.M. Hammond, M.F. Reid, F.S. Richardson, J. Less-Comm. Met. 148 (1989) 311.
[113] C.K. Jayasankar, M.F. Reid, F.S. Richardson, Phys. Status Solidi (b) 155 (1989) 559.
[114] V.V.Ravi Kanth Kumar, C.K. Jayasankar, M.F. Reid, J. Alloys Compd. 193 (1993) 189.
[115] P. Nachimuthu, R. Jagannathan, J. Am. Ceram. Soc. 82 (1999) 387.
[116] G.A. Kumar, R.E. Riman, A.A. Kaminskii, R. Praveena, C.K. Jayasankar, I.K. Bae, S.C. Chae, Y.N. Jang, Phys. Rev. B 74 (2006) 014306.
[117] E.H. Carlson, G.H. Dieke, J. Chem. Phys. 34 (1961) 1602.
[118] C.K. Jayasankar, F.S. Richardson, M.F. Reid, P. Porcher, P. Caro, Inorg. Chim. Acta 139 (1987) 287.
[119] J.B. Gruber, M.E. Hills, T.H. Allik, C.K. Jayasankar, J.R. Quagliano, F.S. Richardson, Phys. Rev. B 41 (1990) 7999.
[120] J.R. Quagliano, F.S. Richardson, J. Alloys Compd. 180 (1992) 131.
[121] J.R. Quagliano, G.W. Burdick, D.P. Glover-Fischer, F.S. Richardson, Chem. Phys. 201 (1995) 321.
[122] C.K. Jayasankar, F.S. Richardson, M.F. Reid, P. Porcher, P. Caro, Inorg. Chim. Acta 139 (1987) 291.
[123] G.W. Burdick, C.K. Jayasankar, F.S. Richardson, M.F. Reid, Phys. Rev. B 50 (1994) 16309.
[124] E. Rukmini, C.K. Jayasankar, M.F. Reid, J. Phys.: Condens. Matter 6 (1994) 5919.
[125] A. Renuka Devi, C.K. Jayasankar, M.F. Reid, Phys. Rev. B 49 (1994) 12551.
[126] J.B. Gruber, B. Zandi, M.F. Reid, Phys. Rev. B 60 (1999) 15643.
[127] K. Rajnak, W.F. Krupke, J. Chem. Phys. 46 (1967) 3532.
[128] G.H. Dieke, B. Pandy, J. Chem. Phys. 41 (1964) 1952.
[129] C.K. Jayasankar, F.S. Richardson, P.A. Tanner, M.F. Reid, Mol. Phys. 61 (1987) 635.
[130] Y.C. Ratnakaram, A. Viswanadha Reddy, R.P.Sreekanth Chakradhar, Spectrochim. Acta Pt. A 58 (2002) 1809.
[131] S.R. Lüthi, H.U. Güdel, M.P. Hehlen, J. Chem. Phys. 110 (1999) 12033.
[132] S.J. Lakshman, Y.C. Ratnakaram, J. Non-Cryst. Solids 94 (1987) 222.
[133] K.W. Krämer, H.U. Güdel, R.N. Schwartz, Phys. Rev. B 56 (1997) 13830.
[134] R. Reisfeld, G. Katz, N. Spector, C.K. Jorgensen, C. Jacoboni, R. De Pape, J. Solid State Chem 41 (1982) 253.
[135] S. Buddhudu, F.J. Bryant, J. Less-Comm. Met. 147 (1989) 213.
[136] B.M. Angelov, J. Alloys Compd. 395 (2005) 48.
[137] W.F. Krupke, J.B. Gruber, J. Chem. Phys. 41 (1964) 1225.
[138] K. Rajnak, B.G. Wybourne, J. Chem. Phys. 41 (1964) 565.
[139] G.H. Dieke, S. Singh, J. Chem. Phys. 35 (1961) 555.
[140] P.A. Tanner, A. De Piante, F.S. Richardson, M.F. Reid, Mol. Phys. 60 (1987) 1037.
[141] C.K. Jayasankar, A. Renuka Devi, E. Rukmini, M.F. Reid, J. Alloys Compd. 193 (1993) 203.
[142] A. Renuka Devi, C.K. Jayasankar, M.F. Reid, J. Alloys Compd. 207/208 (1994) 74.
[143] J.B. Gruber, J.G. Conway, J. Chem. Phys. 32 (1960) 1531.
[144] E.Y. Wong, I. Richman, J. Chem. Phys. 34 (1961) 1182.
[145] B.C. Gerstein, L.D. Jennings, F.H. Spedding, J. Chem. Phys. 37 (1962) 1496.
[146] R.A. Buchanan, K.A. Wickersheim, J.J. Pearson, G.F. Herrmann, Phys. Rev. 159 (1967) 245.
[147] X. Zhou, M.F. Reid, M.D. Faucher, P.A. Tanner, J. Phys. Chem. 110 (2006) 14939.
[148] C.K. Duan, P.A. Tanner, J. Phys. Chem. A 114 (2010) 6055.
[149] P. Dorenbos, J. Andriessen, M. Marsman, C.E. van Eijk, Radiat. Eff. Defects Solids 154 (2001) 237.
[150] R.S. Quimby, Active phenomena in doped halide glasses, in: I.D. Aggarwal, G. Lu (Eds.), Fluoride Glass Fibre Optics, Academic Press, Boston, 1991.
[151] S. Naguleswaran, M.F. Reid, G. Stedman, Mol. Phys. 101 (2003) 917.
[152] A. Edgar, Optical properties of glasses, in: J. Singh (Ed.), Optical Properties of Condensed Matter and Applications, John Wiley & Sons, Chichester, 2006 159p.
[153] B. Henderson, G.F. Imbusch, Optical Spectroscopy of Inorganic Solids, Clarendon Press, Oxford, 1989.
[154] C.K. Duan, M.F. Reid, J. Alloys Compd. 418 (2006) 213.
[155] H.A. Lorentz, The Theory of Electrons and Its Applications to the Phenomena of Light and Radiant Heat, Teubner, Leipzig, 1909.
[156] D. Toptygin, J. Fluoresc. 13 (2003) 201.
[157] F.P. Schuurmans, D.N. de Lang, G.H. Wegdam, R. Sprik, A. Langendijk, Phys. Rev. Lett. 80 (1998) 5077.
[158] F.P. Schuurmans, A. Langendijk, J. Chem. Phys. 113 (2000) 3310.
[159] W. Sellmeier, Ann. Phys. Chem. 219 (1871) 272.
[160] W.T. Carnall, P.R. Fields, K. Rajnak, J. Chem. Phys. 49 (1968) 4412.
[161] F. Auzel, J. Alloys Compd. 380 (2004) 9.
[162] R.D. Peacock, Struct. Bond. 22 (1975) 88.
[163] M.J. Weber, T.E. Varitimos, B.H. Matsinger, Phys. Rev. 8 (1973) 47.
[164] M. Malinowski, R. Wolski, W. Wolinski, Solid State Commun. 74 (1990) 17.
[165] M. Eyal, E. Greenberg, R. Reisfeld, N. Spector, Chem. Phys. Lett. 117 (1985) 108.
[166] J. McDougall, D.B. Hollis, X. Liu, M.B. Payne, Phys. Chem. Glasses 35 (1994) 145.
[167] M. Malinowski, R. Wolski, W. Wolinski, J. Lumin. 35 (1986) 1.
[168] A. Florez, A. Herrera, M. Florez, Phys. Status Solidi C 4 (2007) 4156.
[169] J. McDougall, D.B. Hollis, M.B. Payne, Phys. Chem. Glasses 35 (1994) 258.
[170] A. Florez, M.G. Brik, O. Plata, J. Mater. Sci. Mater. Electron 20 (2009) S230.
[171] F. Auzel, S. Hubert, P. Delamoye, J. Lumin. 26 (1982) 251.
[172] A.A. Kornienko, A.A. Kaminskii, E.B. Dunina, Phys. Status Solidi (b) 157 (1990) 261.
[173] A.A. Kornienko, A.A. Kaminskii, E.B. Dunina, Phys. Status Solidi (b) 157 (1990) 267.
[174] E.B. Dunina, A.A. Kornienko, L.A. Fomicheva, Cent. Eur. J. Phys. 6 (2008) 407.
[175] J.L. Adam, W.A. Sibley, J. Non-Cryst. Solids 76 (1985) 267.
[176] V.R. Kumar, N. Veeraiah, B.A. Rao, S. Buddhudu, J. Mater. Sci. 33 (1998) 2659.
[177] D.E. Henrie, R.L. Fellows, G.R. Choppin, Coord. Chem. Rev. 18 (1976) 199.
[178] C.K. Jorgensen, R. Reisfeld, J. Less-Comm. Met. 93 (1983) 107.
[179] R. Reisfeld, C.K. Jorgensen, Excited state phenomena in vitreous materials, in: K.A. Geschneider Jr, L. Eyring (Eds.), Handbook on the Physics and Chemistry of Rare Earths, vol. 9, North-Holland, Amsterdam, 1987 1p.
[180] S. Tanabe, T. Ohyagi, S. Todoroki, T. Hanada, N. Soga, J. Appl. Phys. 73 (1993) 8451.
[181] S. Tanabe, T. Hanada, T. Ohyagi, N. Soga, Phys. Rev. B 48 (1993) 10591.
[182] M.J. Weber, R.A. Saroyan, R.C. Ropp, J. Non-Cryst. Solids 44 (1981) 137.
[183] T. Izumitani, H. Toratani, H. Kuroda, J. Non-Cryst. Solids 47 (1982) 87.
[184] S. Tanabe, T. Ohyagi, N. Soga, T. Hanada, Phys. Rev. B 46 (1992) 3305.
[185] Y. Nageno, H. Takebe, K. Morinaga, T. Izumitani, J. Non-Cryst. Sol. 169 (1994) 288.
[186] Y. Nageno, H. Takebe, K. Morinaga, J. Am. Chem. Soc. 76 (1993) 3081.
[187] D.J. Singh, Phys. Rev. B 82 (2010) 155145.
[188] J. Murphy, H.H. Caspers, R.A. Buchanan, J. Chem. Phys. 40 (1964) 743.
[189] J.F. van Dijk, M.H. Schuurmans, J. Chem. Phys. 78 (1983) 5317.